ACS OMEGA

Article

Cite This: ACS Omega 2018, 3, 7587−7602

Visible-Light-Driven Photocatalytic Activity of SnO_2−ZnO Quantum Dots Anchored on g-C_3N_4 Nanosheets for Photocatalytic Pollutant Degradation and H_2 Production

S. V. Prabhakar Vattikuti,*,† Police Anil Kumar Reddy,‡ Jaesool Shim,*,† and Chan Byon‡

†School of Mechanical Engineering, Yeungnam University, 214-1 Dae-dong, Gyeongsan 712-749, Gyeongsangbuk-do, Republic of Korea

‡School of Mechanical and Nuclear Engineering, Ulsan National Institute of Science and Technology (UNIST), Ulsan 44919, Republic of Korea

Supporting Information

ABSTRACT: A zero-dimensional/two-dimensional heterostructure consists of binary SnO_2−ZnO quantum dots (QDs) deposited on the surface of graphitic carbon nitride (g-C_3N_4) nanosheets. The so-called SnO_2−ZnO QDs/g-C_3N_4 hybrid was successfully synthesized via an in situ co-pyrolysis approach to achieve efficient photoactivity for the degradation of pollutants and production of hydrogen (H_2) under visible-light irradiation. High-resolution transmission electron microscopy images show the close contacts between SnO_2−ZnO QDs with the g-C_3N_4 in the ternary SnO_2−ZnO QDs/g-C_3N_4 hybrid. The optimized hybrid shows excellent photocatalytic efficiency, achieving 99% rhodamine B dye degradation in 60 min under visible-light irradiation. The enriched charge-carrier separation and transportation in the SnO_2−ZnO QDs/g-C_3N_4 hybrid was determined based on electrochemical impedance and photocurrent analyses. This remarkable photoactivity is ascribed to the "smart" heterostructure, which yields numerous benefits, such as visible-light-driven fast electron and hole transfer, due to the strong interaction between the SnO_2−ZnO QDs with the g-C_3N_4 matrix. In addition, the SnO_2−ZnO QDs/g-C_3N_4 hybrid demonstrated a high rate of hydrogen production (13 673.61 μmol g^{-1}), which is 1.06 and 2.27 times higher than that of the binary ZnO/g-C_3N_4 hybrid (12 785.54 μmol g^{-1}) and pristine g-C_3N_4 photocatalyst (6017.72 μmol g^{-1}). The synergistic effect of increased visible absorption and diminished recombination results in enhanced performance of the as-synthesized tin oxide- and zinc oxide-modified g-C_3N_4. We conclude that the present ternary SnO_2−ZnO QDs/g-C_3N_4 hybrid is a promising electrode material for H_2 production and photoelectrochemical cells.

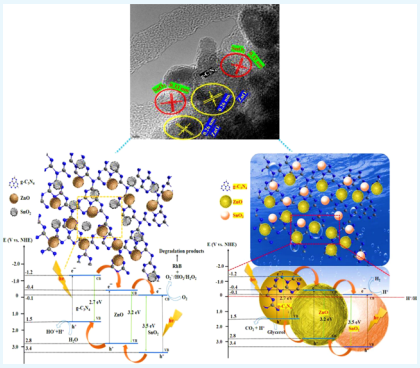

1. INTRODUCTION

The need to solve the global energy crisis and environmental concerns has led researchers to work on the development of the hydrogen economy. Economically feasible strategies for high-yield hydrogen production remain critically important for the extensive use of hydrogen as an energy source.[1,2] Hydrogen is regarded as a green energy source and a promising environmentally friendly alternative to fossil fuels. Various approaches have been proposed for the production of hydrogen using solar energy. Artificial photosynthesis has attracted significant research efforts because of its unique potential.

To date, considerable research attention and efforts have focused on visible-light-active metal-free photocatalysts for the degradation of organic pollutants and H_2 production because of the increasing need for environmental care and clean energy harvesting.[3] Several photocatalysts have been investigated, including TiO_2,[4] graphitic carbon nitride (g-C_3N_4),[5,6] ZnO,[7,8] SnO_2,[9,10] and MoS_2.[11] Among these, g-C_3N_4 has gained prominence as a suitable candidate for both photocatalytic dye degradation and water splitting because of its well-suited band gap of ca. 2.7 eV that facilitates superior excitation of charge carriers by efficient absorption of sunlight. In other words, of the various two-dimensional (2D) materials studied so far, g-C_3N_4 is considered to be the most promising candidate given its low cost, stability, inertness, and, especially, its suitable band gap energy.[12] More significantly, g-C_3N_4-based nanomaterials are often applied in photocatalyst applications because they can satisfy the current environmental requirements of "green" photocatalysts in hybrid heterostructures, analogue to commercial TiO_2-based photocatalysts. However, g-C_3N_4 has a low photocatalytic efficiency, which arises from the recombination of photoinduced electron and hole pairs.[13] Interestingly, the conduction band (CB) potential of g-C_3N_4 is more negative than the reduction potential of H_2O/H_2, which is encouraging, suggesting that it can be used to reduce protons to H_2.[14] However, the H_2 production efficiency in photocatalytic water

Received: March 13, 2018
Accepted: June 5, 2018
Published: July 10, 2018

DOI: 10.1021/acsomega.8b00471
ACS Omega 2018, 3, 7587−7602

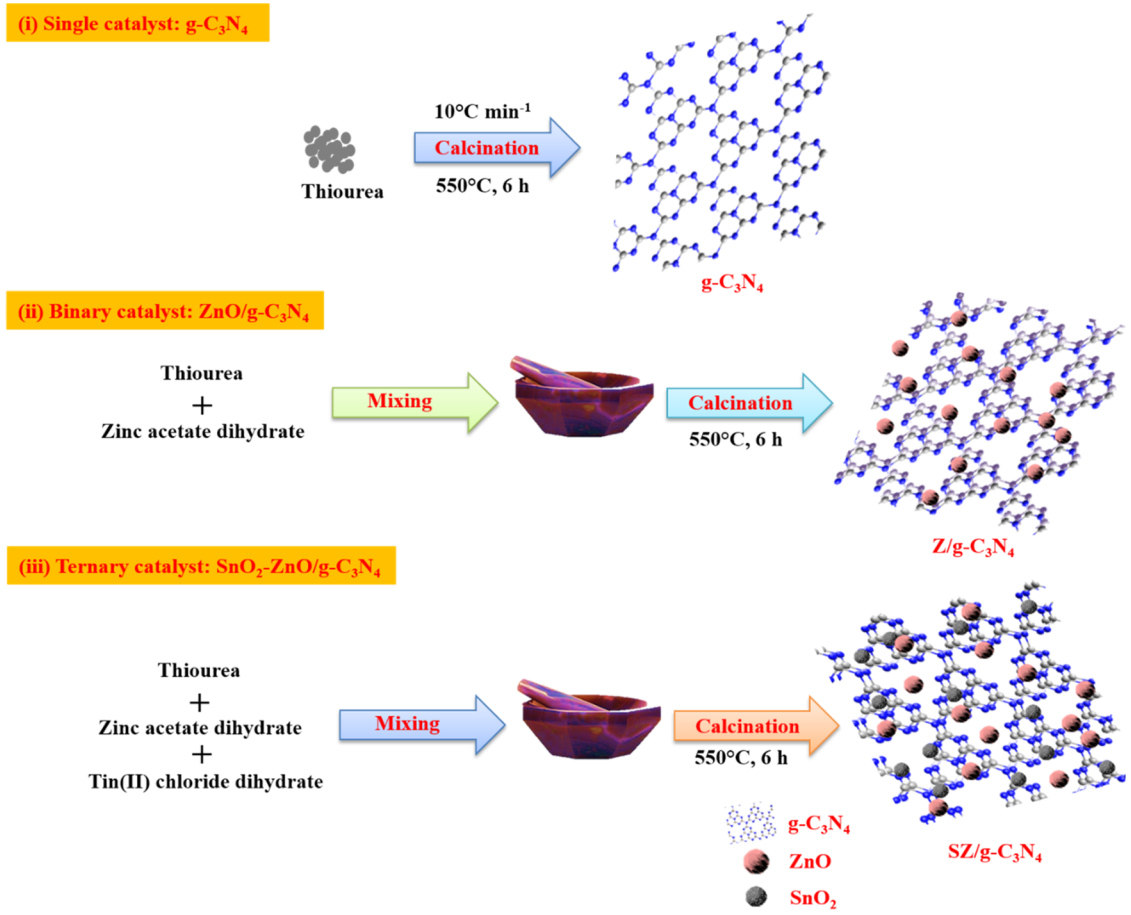

Figure 1. Schematic synthetic procedure for the formation of SZ/g-C_3N_4 heterostructure.

splitting attained to date is far lower than that required for practical application. This is due to the fast recombination of electron−hole pairs and their susceptibility to photocorrosion in the photocatalysts.[15] Therefore, existing photocatalysts must be modified to improve their activity. Modifications can include loading of co-catalysts, coupling of two or three materials, and doping with a metal phase. Among these, one successful approach is the introduction of co-catalysts onto the surface of photocatalysts.[16] A co-catalyst is usually essential to trap the photogenerated electrons from the surface of the photocatalyst. However, although this modification does not entirely diminish electron−hole recombination, it can moderate the energy required for the surface active reactions. In most studies, noble metals are usually considered as co-catalyst candidates.[17,18] However, it is essential to develop noble-metal-free catalysts because of their high cost and scarcity, which impede their widespread use. Therefore, preparation of photocatalysts using earth-abundant metals and their compounds is an attractive alternative.

One common strategy is to combine two or three kinds of semiconductor materials by coupling g-C_3N_4 with metal oxide materials, such as SnO_2, ZnO, ZnO, or TiO_2,[19−22] by virtue of their highly efficient photoactivity performance and remarkable recycling stability. These ternary heterostructured visible-light-driven photocatalysts have attracted intense interest for their combined benefits, i.e., high specific surface area and fast photoinduced electron and hole transfer with favorable interface features. A key point in the development of heterostructured photocatalysts is the design and synthesis of photocatalysts with efficient photoactive efficiency and cycling stability. Recent reports have demonstrated that the combination of metal oxide nanomaterials with g-C_3N_4 can greatly enhance the photocatalytic performance.[23,24] For example, Shen et al.[24] reported the integration of SnO_2/g-C_3N_4 crystals as core−shell structures, which endowed the hybrids with efficient photocatalytic behaviors for degradation of pollutants. It is widely known that the specific surface area of g-C_3N_4 depends on the synthetic conditions. However, a critical challenge in the synthesis of g-C_3N_4 is to obtain a-few-layer to monolayer g-C_3N_4 with weak van der Waals forces between the adjacent layers

In this work, we establish a synthetic procedure for ternary SnO_2−ZnO/g-C_3N_4 heterostructured hybrids, in which SnO_2−ZnO quantum dots (QDs) are anchored on g-C_3N_4 nanosheets via a facile in situ co-pyrolysis approach. This procedure forms an intriguing zero-dimensional (0D)/2D heterostructure. In this architecture, SnO_2/ZnO QDs were used as spacers between the g-C_3N_4 layers, forming a three-dimensional conductive network that facilitates fast electron and hole transport. In addition, the as-designed heterostructures also provide a porous structure that may diminish the recombination of photoinduced electrons and holes and also act as absorbents for the pollutant molecules on the hybrid surface. The resulting hybrids exhibited excellent photocatalytic performance under visible-light irradiation with outstanding cycling stability.

DOI: 10.1021/acsomega.8b00471
ACS Omega 2018, 3, 7587−7602

2. RESULTS AND DISCUSSION

The synthetic steps for the resulting hybrids are illustrated in Figure 1. The typical synthetic procedure for the synthesis of the SZ/g-C_3N_4 hybrid is discussed in Experimental Section. A one-step method was used to produce highly crystalline monodispersed SnO_2−ZnO nanoparticles on the surface of few-layer graphitic carbon nitride (g-C_3N_4) sheets. As illustrated in the first step of Figure 1, the g-C_3N_4 sheets have abundant functional groups on their surface. These functional groups are assumed to be uniformly distributed on the g-C_3N_4 surface and play a vital role in the formation of the heterojunction. The g-C_3N_4 sheets can be easily separated in ethanol, forming highly dispersed few-layer sheets in solution because of these functional species. When the solution of g-C_3N_4 sheets is mixed with a zinc acetate or $SnCl_2$ solution, the Zn^{2+} or Sn^{2+} ions selectively bond with functional groups by electrostatic interactions. Because g-C_3N_4 is highly dispersed and the Zn^{2+} or Sn^{2+} ions are in excess, all of the g-C_3N_4 sheets are saturated with Zn^{2+} or Sn^{2+} ions. During the co-pyrolysis process in a furnace, the Zn^{2+} or Sn^{2+} ions are spontaneously converted to ZnO or SnO_2 nanoparticles, which are bonded to the surface of g-C_3N_4 through the functional groups attached on the surface of g-C_3N_4 like −OH or −COOH.[25,26] For instance, $Zn(OH)_2$ reacts with g-C_3N_4−OH or g-C_3N_4−COOH and forms Zn−O−g-C_3N_4 or Zn−O−OC−g-C_3N_4.

The X-ray diffraction (XRD) patterns of pristine g-C_3N_4, ZnO, Z/g-C_3N_4, SnO_2, and SZ/g-C_3N_4 hybrid are shown in Figure 2. All of the diffraction peaks of the pristine samples of g-C_3N_4, ZnO, and SnO_2 correspond to monoclinic g-C_3N_4 (JCPDS no. 37-1526),[25] hexagonal wurtzite ZnO (JCPDS no. 36-1451),[27,28] and rutile tetragonal SnO_2 (JCPDS no. 41-1445),[29] respectively. For pure g-C_3N_4, the two distinct XRD peaks at 12.89 and 27.45° correspond to the (100) and (002) planes of the graphitic carbon nitride. Interestingly, distinct peaks at 31.77, 34.11, 36.15, 47.46, 56.73, 62.9, and 67.53°, corresponding to the (100), (002), (101), (102), (110), (103), and (112) crystal planes of ZnO nanoparticles, were observed in the Z/g-C_3N_4 hybrid. In the case of the SZ/g-C_3N_4 hybrid, additional peaks at 25.86, 33.57, and 51.33° corresponding to the (110), (101), and (211) crystal planes of SnO_2 were observed in addition to the Z/g-C_3N_4 hybrid peaks, which indicates that this is a combined phase of the g-C_3N_4, SnO_2, and ZnO materials in the SZ/g-C_3N_4 hybrid and confirms that the SnO_2−ZnO/g-C_3N_4 hybrid had been successfully synthesized. In addition, no other characteristic impurity peaks were observed in the XRD patterns.

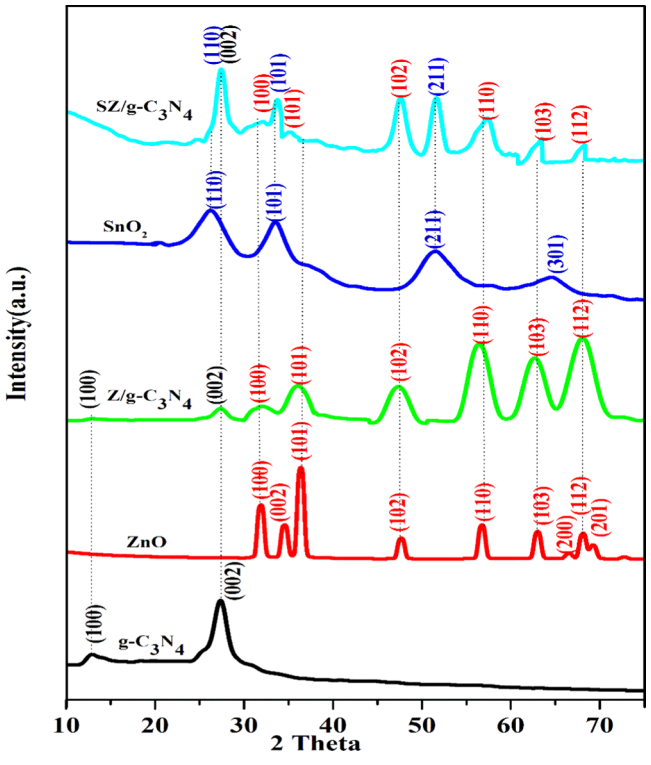

Figure 2. XRD patterns of pristine g-C_3N_4, ZnO, Z/g-C_3N_4, SnO_2, and SZ/g-C_3N_4 catalysts.

The transmission electron microscopy (TEM) and high-resolution TEM (HRTEM) images of pure g-C_3N_4 and the Z/g-C_3N_4 hybrid are shown in Figure S1. Figure S1a shows only one morphology: the two-dimensional (2D) layered structure of pristine g-C_3N_4 that acts as a substrate/platform for the deposition of foreign materials. Figure S1b−d shows high-magnification TEM images of the Z/g-C_3N_4 hybrid. The ZnO QDs are randomly distributed on the surface of the g-C_3N_4 nanosheets. The crystallographic spacings were determined to be 0.33 and 0.26 nm, which agree well with the (002) *d*-spacings of g-C_3N_4 and ZnO. This result indicates that the ZnO QDs had been successfully synthesized over the surface of g-C_3N_4. HRTEM images of the SZ/g-C_3N_4 hybrid are shown in Figure 3. As shown in the high-magnification HRTEM images (Figure 3a−c), there is an obvious contrast between the SnO_2 and ZnO QDs on the top surface of the g-C_3N_4 nanosheets, as marked by the yellow circles, indicating the SnO_2 and ZnO materials. In addition, it is clear that the molar ratio of SnO_2 and ZnO affects the intensity of the QDs on the g-C_3N_4 nanosheets, which can be easily varied. As shown in Figure 3c, the interplanar distances of the SnO_2 and ZnO QDs were measured to be 0.33 and 0.26 nm, respectively, which are consistent with the literature for (110) SnO_2 and (002) ZnO.[30] In addition, the electron diffraction patterns shown in Figure 3d, which were recorded at positions randomly chosen on the surface of hybrid, has a polycrystalline nature. In detail, the selected area electron diffraction (SAED) pattern of the SZ/g-C_3N_4 hybrid displays two types of diffraction features: one set of isolated dots originating from the g-C_3N_4 sheets and another set from SnO_2−ZnO nanocrystals. This is clear evidence for the formation of the SZ/g-C_3N_4 hybrid structure. Figure 4a−f reveals the even distribution of the C, N, Sn, Zn, and O elements and verifies the successful preparation of the SZ/g-C_3N_4 composite. The constituents of SnO_2 and ZnO on g-C_3N_4 are C, N, Sn, Zn, and O, as shown in Figure 4g. In addition, HRTEM-energy-dispersive X-ray (EDX) also confirmed the formation of SnO_2 and ZnO nanoparticles on the surface of the g-C_3N_4 nanosheets.

In addition, the morphology, elemental mapping, and EDX analysis of the SZ/g-C_3N_4 hybrid were carried out using scanning electron microscopy (SEM), as shown in Figure S2. Similar to the morphology observed in the HRTEM images, tiny SnO_2 and ZnO nanoparticles can be seen randomly distributed on the surface of the g-C_3N_4 nanosheets (Figure S2a). Figure S2b−f reveals the existence of C, N, Sn, Zn, and O distributed randomly over the entire architecture. The SEM and HRTEM elemental mapping and EDX results clearly show that the 0D/2D SnO_2−ZnO nanoparticles/g-C_3N_4 nanosheets hybrid had been successfully synthesized. Figure S3 presents SEM-EDX spectra of pristine g-C_3N_4, Z/g-C_3N_4, and SZ/g-

DOI: 10.1021/acsomega.8b00471
ACS Omega 2018, 3, 7587−7602

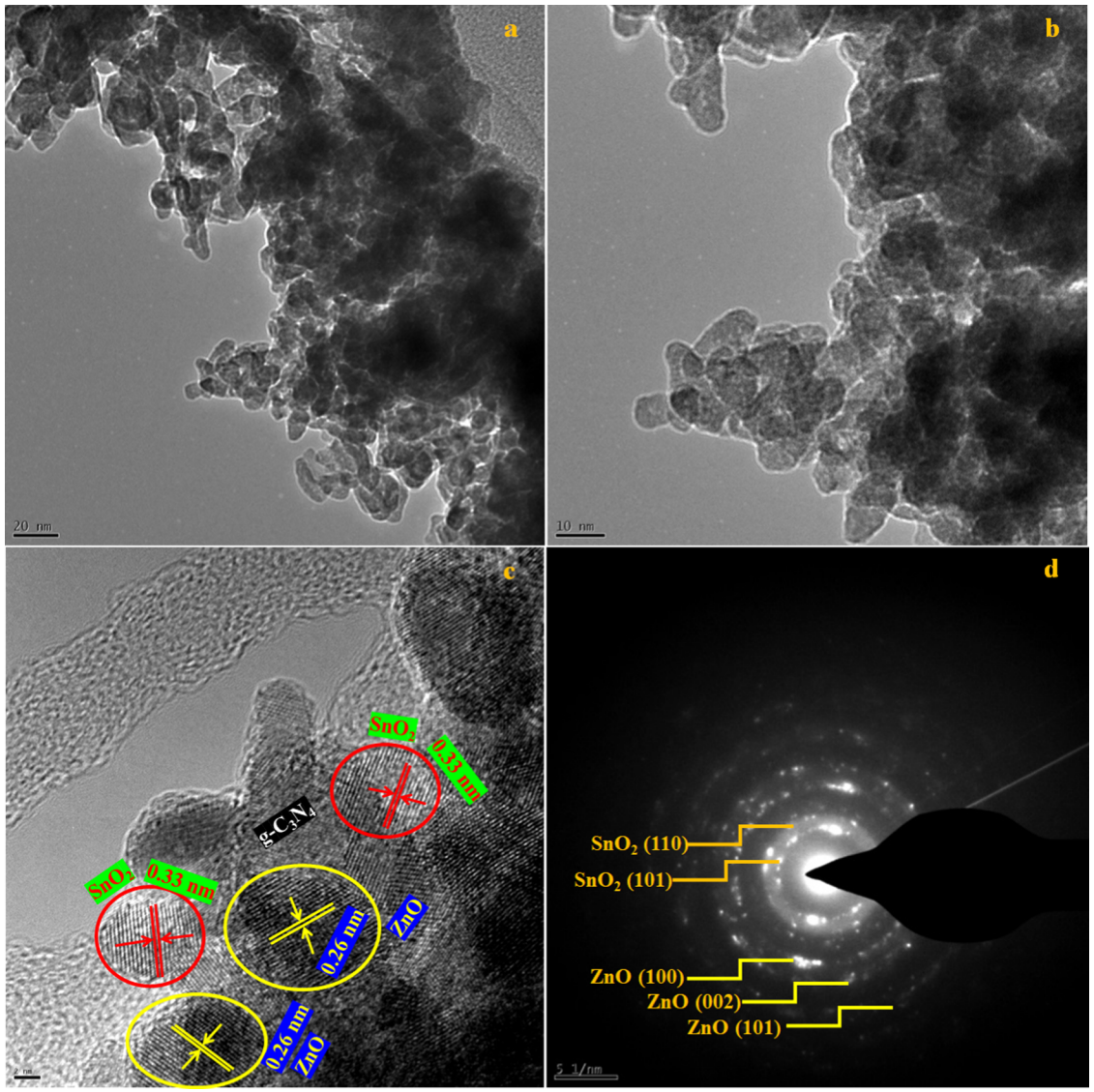

Figure 3. (a–c) HRTEM images and (d) SAED pattern of the SZ/g-C_3N_4 catalyst.

C_3N_4 catalysts. The table provided in the inset gives the surface composition of C, N, O, Zn, and Sn elements. The wt % values of Sn and Zn on the surface of SZ/g-C_3N_4 composite were observed to be 3.79 and 14.79, respectively. In addition to the EDX analysis by SEM, the inductively coupled plasma-optical emission spectroscopy (ICP-OES) analysis (Figure S4) of the SZ/g-C_3N_4 nanocomposite is performed to find the bulk composition of Sn and Zn. The results show the wt % values of Sn and Zn in the ternary SZ/g-C_3N_4 nanocomposite to be 1.99 and 26.56, respectively. Interestingly, the bulk composition of the Sn and Zn elements observed by the ICP-OES is lower than the surface composition of the Sn and Zn elements experimented by the SEM-EDX. This clarifies that the Sn and Zn elements are present more on the surface rather to the bulk. This attributes that the SnO_2 and ZnO nanoparticles are highly dispersed over the surface of g-C_3N_4 sheets.

The Fourier transform infrared (FTIR) spectra of pure g-C_3N_4 and the Z/g-C_3N_4 and SZ/g-C_3N_4 hybrids are shown in Figure 5. For the pure g-C_3N_4 sample, broad peaks at 3088, 1603, 1405, 1317, and 1238 cm^{-1} are attributed to the stretching vibrations of N–H and O–H bonds, stretching vibrations of aromatic C–N heterocycles composed of trigonal N–C_3 and C–NH–C bridging units, and the formation of C–N–C bonds, respectively.[31] The peaks from 580 to 1100 cm^{-1} could be ascribed to the breathing mode of the tri-*s*-triazine ring.[31] In the case of the Z/g-C_3N_4 and SZ/g-C_3N_4 hybrid samples, similar absorption bands were observed, including the main characteristic peaks of pure g-C_3N_4. The peaks in the range of 1200–1410 cm^{-1} are assigned to the C–N and C=N stretching vibration modes obtained from the characteristic peaks of g-C_3N_4. For the nanocomposites, the broad absorption band at 2900–3700 cm^{-1} is attributed to the terminal NH_2 or NH groups at the defect sites of the g-C_3N_4 aromatic rings.[31−34] The characteristic peaks of g-C_3N_4 are present in both Z/g-C_3N_4 and SZ/g-C_3N_4 nanocomposites.

The active sites and high surface area of the photocatalysts have a significant effect on the photocatalytic activities. The specific surface areas of all photocatalysts were measured using the nitrogen adsorption–desorption curves. Figure 6 shows the N_2 adsorption–desorption isotherms and pore size distribution of g-C_3N_4 and the Z/g-C_3N_4 and SZ/g-C_3N_4 hybrids. The SZ/g-C_3N_4 nanocomposite has a higher specific Brunauer–Emmett–Teller (BET) surface area of 46.38 $m^2\ g^{-1}$ and pore volume of 0.234 $cm^3\ g^{-1}$ than those of pristine g-C_3N_4 (24.7 m^2

DOI: 10.1021/acsomega.8b00471
ACS Omega 2018, 3, 7587–7602

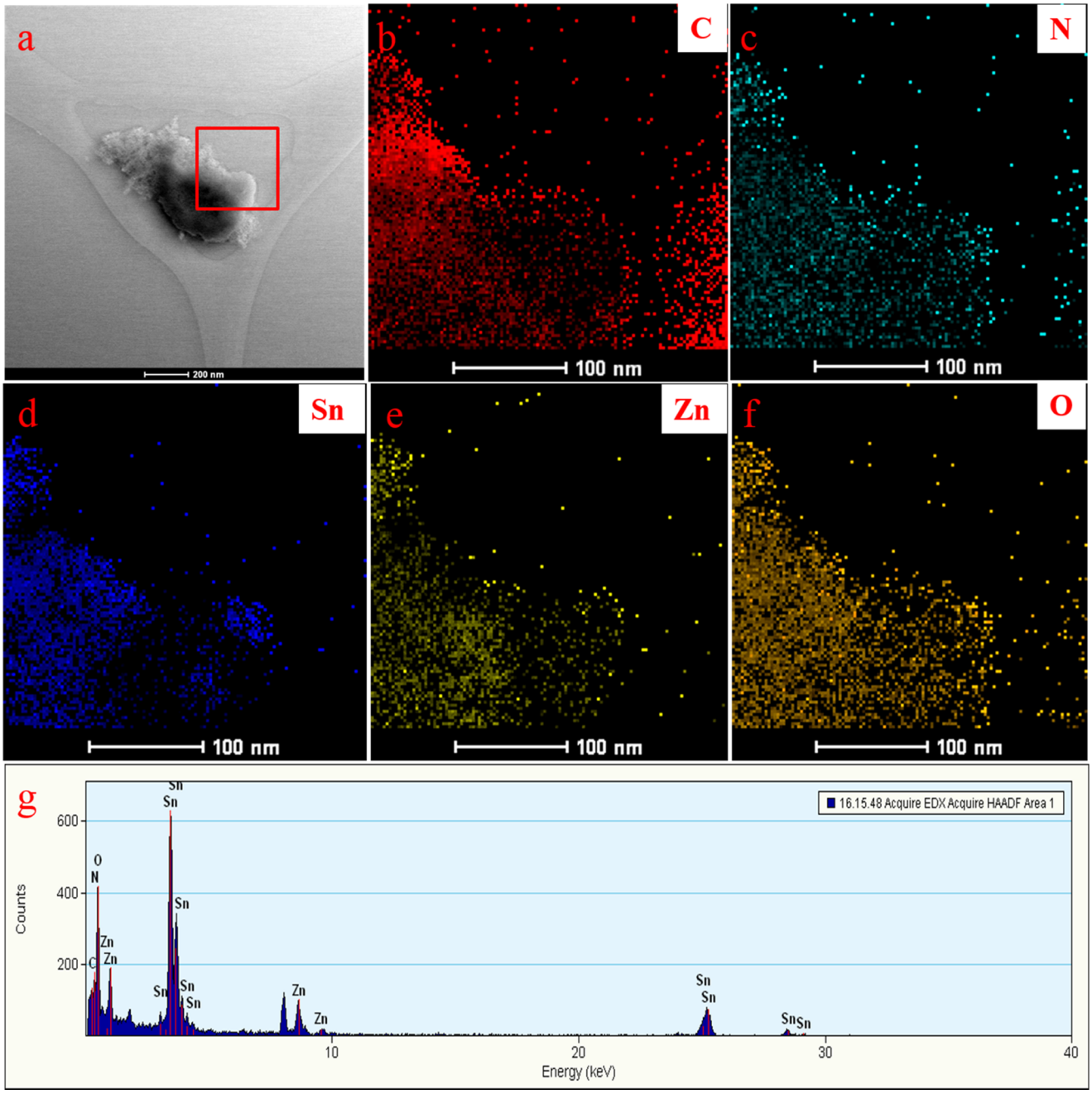

Figure 4. (a) HRTEM image and HRTEM-EDX mapping of (b) C, (c) N, (d) Sn, (e) Zn, (f) O elements, and (g) HRTEM-EDX of the SZ/g-C_3N_4 catalyst.

g^{-1} and 0.098 cm^3 g^{-1}, respectively) and Z/g-C_3N_4 (34.65 m^2 g^{-1} and 0.181 cm^3 g^{-1}, respectively). A distinct hysteresis loop for the SZ/g-C_3N_4 nanocomposite is present, which is typical of mesoporous materials. This structure is favorable for the photodegradation of pollutants and is not present in pristine g-C_3N_4. The surface areas of the materials increased in the following order: pristine g-C_3N_4 < Z/g-C_3N_4 < SZ/g-C_3N_4. Commonly, the surface area of the nanocomposite is higher than that of the components, as reported for several composite photocatalysts.[30,31,35] For instance, in our previous work,[25] we constructed novel MoS_2/Al_2O_3/g-C_3N_4 heterojunction photocatalysts and reported BET surface areas of 24.2 m^2 g^{-1} for g-C_3N_4 and 101.5 m^2 g^{-1} for MoS_2/Al_2O_3/g-C_3N_4.

To further confirm the elemental compositions of the obtained samples, X-ray photoelectron spectroscopy (XPS) patterns of the prepared samples were obtained, as shown in Figure 7. Figure 7a shows the survey XPS image of the SZ/g-C_3N_4 hybrid; it indicates that SZ/g-C_3N_4 contains C, N, O, Sn, and Zn. Figure 7b shows the XPS image of Sn 3d for the SZ/g-C_3N_4 hybrid. The peaks at binding energies of 487.31 and 495.76 eV correspond to Sn^{2+} and Sn^{4+}, respectively.[36] The XPS analyses indicate that both Sn^{2+} and Sn^{4+} species exist in the composite. Figure 7c shows the observed peaks, which can be assigned to ZnO (Zn) at 1020.98 and 1045.54 eV for Zn $2p_{3/2}$ and Zn $2p_{1/2}$, respectively, and is consistent with the literature.[7] From Figure 7d, there are three main distinctive peaks of the C 1s core level of g-C_3N_4 at 284.32, 285.88, and

DOI: 10.1021/acsomega.8b00471
ACS Omega 2018, 3, 7587−7602

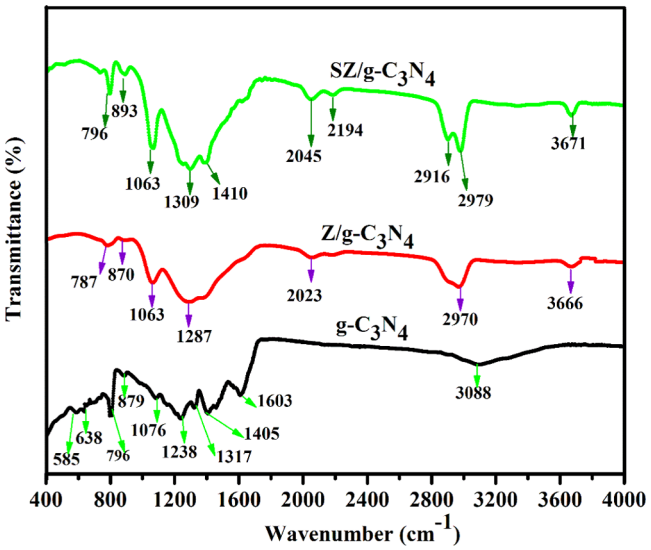

Figure 5. FTIR spectra of pristine g-C_3N_4, Z/g-C_3N_4, and SZ/g-C_3N_4 catalysts.

287.87 eV, which were assigned to the sp^2 C−C bonds of graphitic carbon, sp^3-coordinated carbon bonds, and sp^2-bonded carbon (N−C═N) in the tri-*s*-triazine rings, respectively.[25] Figure 7e shows the N 1s peaks at 398.36 and 400.49 eV, which can be ascribed to sp^2-bonded N (C−N═C) and amino groups (C−N−H) of g-C_3N_4, respectively.[25] Figure 7f shows the O 1s spectrum of the SZ/g-C_3N_4 hybrid. The peak at 530.75 eV is ascribed to the lattice oxygen in the normal metal oxide crystal structure, and the high energy peak at 532 eV is attributed to surface-adsorbed hydroxy groups. Further, the XPS images confirm that the 0D SnO_2−ZnO-nanoparticle-loaded 2D g-C_3N_4 nanosheets and the formed 0D/2D SZ/g-C_3N_4 heterojunctions exhibited improved stability and photocatalytic activity.

The UV−vis absorption spectra of the g-C_3N_4, Z/g-C_3N_4, and SZ/g-C_3N_4 catalysts are shown in Figure 8. They show that the deposition of ZnO and SnO_2 on the g-C_3N_4 resulted a strong absorption band around 400−500 nm, which matches well with the visible part of the solar spectrum. Using the ultraviolet−visible (UV−vis) diffuse reflection spectrum (DRS), the band gaps of all samples were estimated according to the equation $E_g = 1240/\lambda$, where E_g is the band gap energy and λ is the absorption wavelength.[37] The absorption onsets were observed at approximately 459, 455, and 450 nm for the g-C_3N_4, Z/g-C_3N_4, and SZ/g-C_3N_4 photocatalysts, respectively. The SZ/g-C_3N_4 had better photoresponse and absorption intensity than g-C_3N_4 and Z/g-C_3N_4 samples. By the introduction of ZnO and SnO_2 into g-C_3N_4, a slight blue shift in the absorption edge was observed compared to the pristine g-C_3N_4 owing to the increased variation in the optical absorption of the nanocomposite. The increase in optical absorption results from quantum confinement, and this is the reason for the blue shift in the composite samples, which is consistent with the XRD results. Moreover, the ZnO and SnO_2 nanoparticles dispersed over the surface of the g-C_3N_4 inhibit the agglomeration of the g-C_3N_4 nanosheets. The optical properties of the exfoliated nanosheets of the g-C_3N_4 are different from those of the bulk g-C_3N_4 sheets. Hence, these combined effects enhance the absorption of low-energy photons and, consequently, increase the number of photo-excited charges.

2.1. Photocatalytic Degradation of Rhodamine B (RhB) Dye. The photocatalytic activities of g-C_3N_4 and the Z/g-C_3N_4 and SZ/g-C_3N_4 nanocomposites were estimated using RhB dye degradation in aqueous solutions. The time-dependent UV−vis absorption spectra of RhB dye degradation over g-C_3N_4 and the Z/g-C_3N_4 and SZ/g-C_3N_4 nanocomposites are shown in Figure S5. Figure S5a−c shows the variation in the RhB absorption with irradiation time over different photocatalysts. The decrease in the intensity of the absorption spectra of RhB dye (λ_{max} = 553 nm) at different intervals of irradiation time over g-C_3N_4 and the Z/g-C_3N_4 and SZ/g-C_3N_4 nanocomposites was observed in detail. The reduction in the peak intensities is an evidence of the photodegradation of RhB in the presence of the photocatalysts (Figure S5a−c). The complete degradation of the RhB dye under visible-light irradiation in the presence of g-C_3N_4, Z/g-C_3N_4, and SZ/g-C_3N_4 was achieved after 130, 100, and 60 min

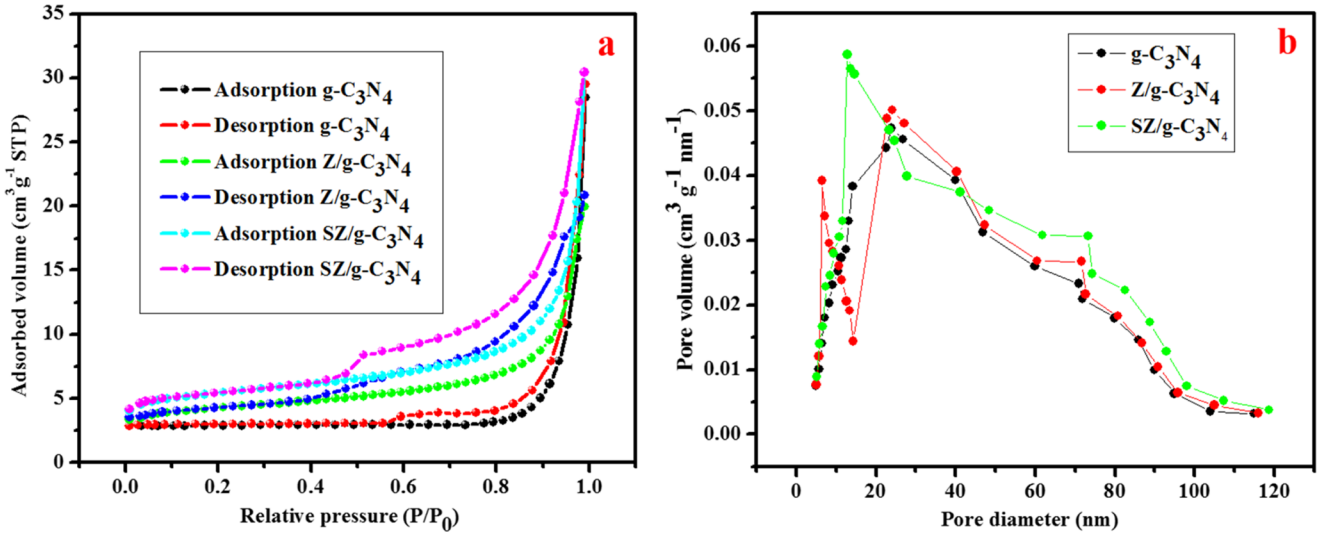

Figure 6. (a) N_2 adsorption/desorption isotherms and (b) Barrett−Joyner−Halenda pore size distribution data of pristine g-C_3N_4, Z/g-C_3N_4, and SZ/g-C_3N_4 catalysts.

DOI: 10.1021/acsomega.8b00471
ACS Omega 2018, 3, 7587−7602

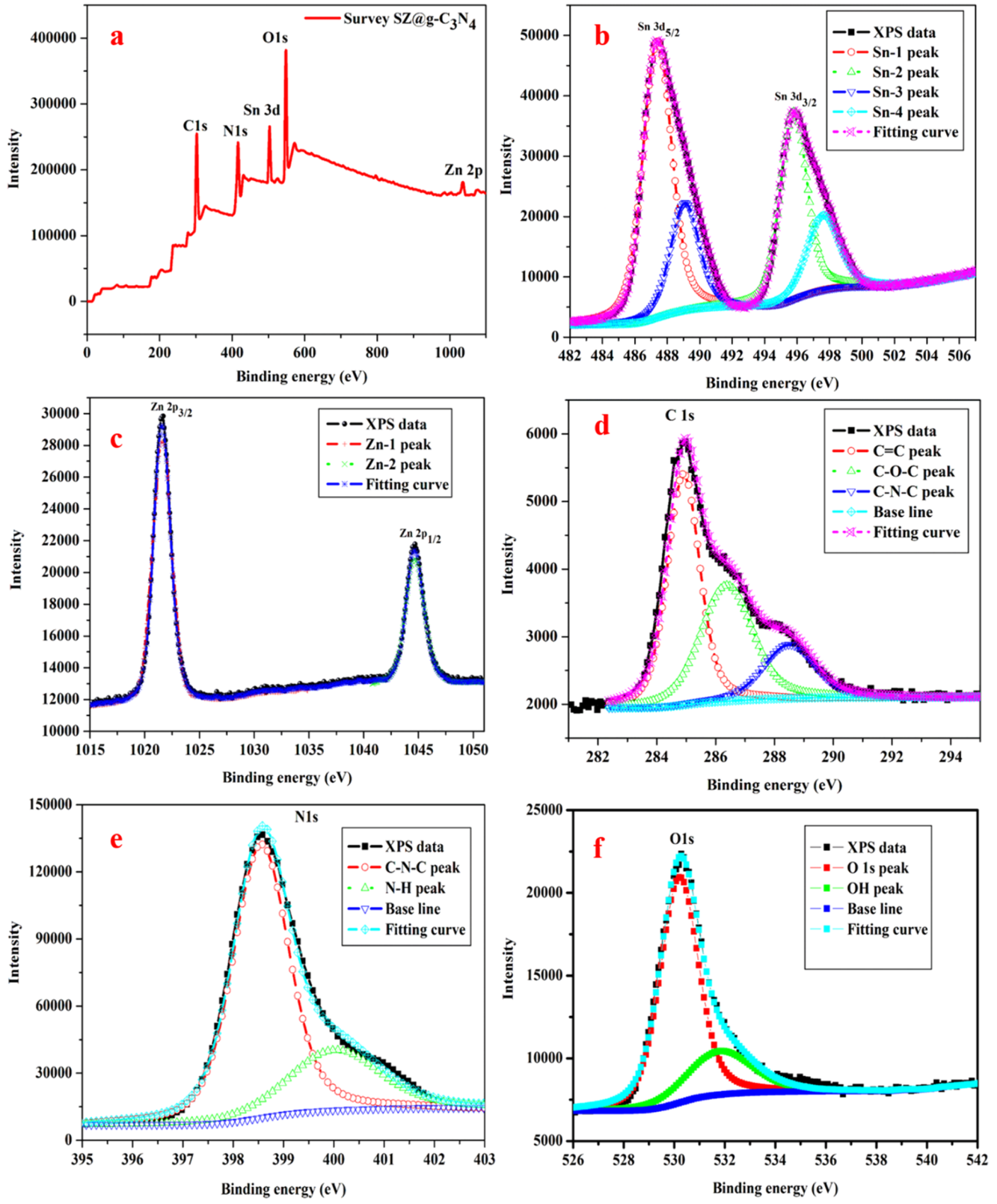

Figure 7. (a) XPS and high-resolution patterns for (b) Sn, (c) Zn, (d) C, (e) N, and (f) O of the SZ/g-C_3N_4 catalyst.

irradiation, respectively. Unsurprisingly, the ternary nanocomposite (SZ/g-C_3N_4) demonstrated better performance than both g-C_3N_4 and the Z/g-C_3N_4 nanocomposite. Figure 9 shows the comparison of the photocatalytic performances of different photocatalysts. Photodegradation depends on (i) the adsorption of the dye by the photocatalyst, (ii) the presence of fast charge-carrier exchange pathways, and (iii) a large number of highly active surface sites. In this study, g-C_3N_4 acts as an adsorption support material and dye is adsorbed on the surface of the 2D nanosheets. The ability of g-C_3N_4 as a good adsorbent for organic compounds is because of the favorable interactions between the dye molecules and the aromatic

DOI: 10.1021/acsomega.8b00471
ACS Omega 2018, 3, 7587−7602

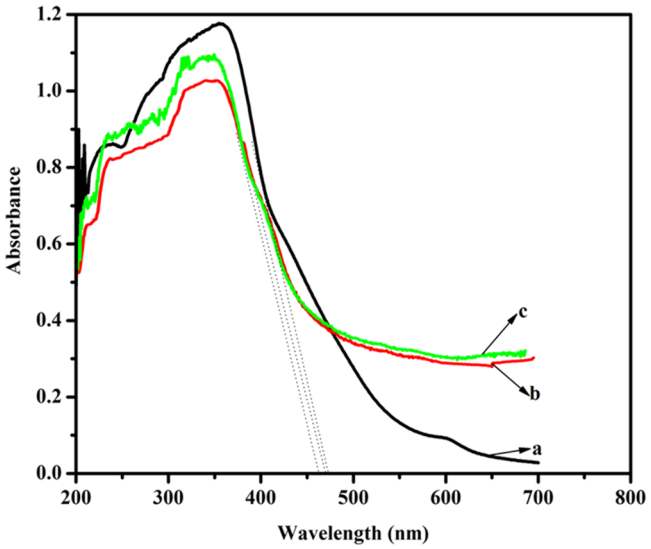

Figure 8. UV−vis spectra of (a) pristine g-C_3N_4, (b) Z/g-C_3N_4, and (c) SZ/g-C_3N_4 catalysts.

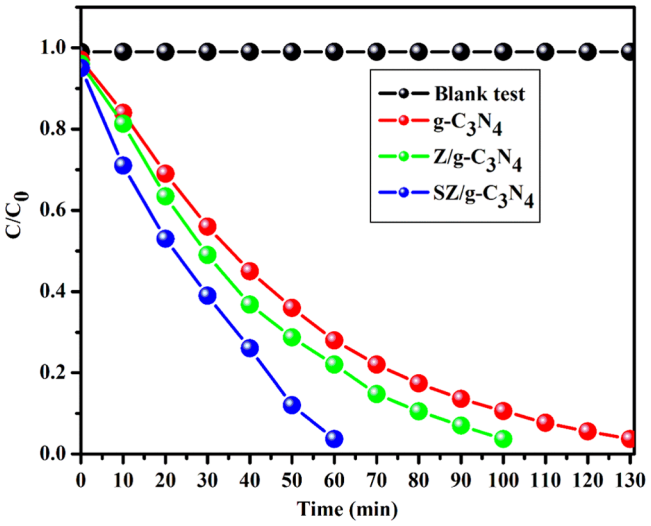

Figure 9. Photocatalytic activities of different photocatalysts for the degradation of RhB under visible-light irradiation.

structure of g-C_3N_4.[38] Also, the extended delocalization of π electrons in g-C_3N_4 allows the charge carriers to have a high mobility. However, the bare g-C_3N_4 demonstrated lower photocatalytic activity because of the recombination of charge carriers. Z/g-C_3N_4 shows better performance than pristine g-C_3N_4 owing to the contribution of ZnO quantum-sized nanoparticles, which reduces the charge-carrier recombination in g-C_3N_4. The SZ/g-C_3N_4 ternary nanocomposite demonstrated excellent performance compared to g-C_3N_4 and the Z/g-C_3N_4 nanocomposite. The quantum-sized SnO_2 and hexagonal wurtzite ZnO nanoparticles actively contribute to significantly improved photocatalytic activity. The SZ/g-C_3N_4 ternary nanocomposite showed greatly improved photocatalytic activity because of the improved light absorption and transfer of photoinduced charge carriers arising from the combination of the benzene aromatic structure of g-C_3N_4 with the SnO_2 and ZnO QDs. Recently, Dong et al. have reported that g-C_3N_4 shows extraordinary performance as a photocathode for photoelectrochemical hydrogen production[39] and degradation of heavy metals[40] under visible-light irradiation. This is an additional advantage because organic species are trapped on the high surface area of the nanosheets; thus, ZnO and SnO_2 in the vicinity can efficiently degrade the adsorbed RhB dye. The holes and electrons initiate an oxidative pathway, and, consequently, the adsorbed RhB dye is oxidized. Thus, photoactive radicals are created during the reaction, which convert into carbonaceous products, such as CO_2 and other intermediates. The photocatalysis reaction observes pseudo-first-order reaction kinetics according to the Langmuir−Hinshelwood model[41] as follows

$$C = C_0\, e^{-kt} \quad (1)$$

$$\ln C/C_0 = -kt \quad (2)$$

where k, C_0, and C are the pseudo-first-order kinetic constant and the initial and final concentrations, respectively. The kinetic plots and apparent rate constants (K, i.e., the slope) of the g-C_3N_4, Z/g-C_3N_4, and SZ/g-C_3N_4 nanocomposites are shown in Figure 10a−c. For all degradation experiments, the best fit for the kinetic order was obtained with the first-order equation. The SZ/g-C_3N_4 ternary nanocomposite is 5.11 and 2.12 times more efficient than g-C_3N_4 and the Z/g-C_3N_4 nanocomposite, respectively. The reaction constants for g-C_3N_4 and the Z/g-C_3N_4 and SZ/g-C_3N_4 nanocomposites were estimated to be 0.0036, 0.0087, and 0.0184 min^{-1}, respectively (Figure 10d). Thus, the SZ/g-C_3N_4 nanocomposite has higher photocatalytic efficiency than the other nanocomposites owing to the synergistic effect of the three components, i.e., g-C_3N_4, ZnO, and SnO_2.

To understand the effects of ZnO and SnO_2 on the separation of electron−hole pairs in the g-C_3N_4 nanosheets, the photoluminescence (PL) spectra of all samples were analyzed. Figure 11 shows the PL spectra of g-C_3N_4, Z/g-C_3N_4, and SZ/g-C_3N_4 samples. Pure g-C_3N_4 has the strongest peak around 442 nm. For the Z/gC_3N_4 sample, the emission intensity decreased considerably, signifying that the ZnO-anchored g-C_3N_4 nanosheet has lower recombination rate for the photoinduced charge carriers. However, the SZ/g-C_3N_4 sample demonstrated the lowest intensity in its spectrum, signifying much more suppression for recombination of the photoinduced electron−hole pairs. Therefore, the result of PL spectra exhibited that an important reason for the improved photocatalytic activities of Z/g-C_3N_4 and SZ/g-C_3N_4 is the effective separation of the electron−hole pairs, owing to the matching of the energy levels of g-C_3N_4, ZnO, and SnO_2 materials and similar results reported in the literature.[32]

Figure 12 presents a plausible mechanism for RhB degradation using the SZ/g-C_3N_4 nanocomposite. In the ternary SZ/g-C_3N_4 nanocomposite, the conduction band potential of g-C_3N_4 (−1.2 eV vs normal hydrogen electrode (NHE)) is more negative than the conduction band potentials of ZnO (−0.4 eV vs NHE) and SnO_2 (−0.1 eV vs NHE). Hence, the transfer of photogenerated electrons from g-C_3N_4 to ZnO and SnO_2 is thermodynamically feasible. During the visible-light irradiation of the SZ/g-C_3N_4 nanocomposite, the photogenerated electrons are transferred from the conduction band (CB) of g-C_3N_4 to the CB of SnO_2 via the CB of ZnO, whereas the photogenerated holes transfer to the valence band (VB) of g-C_3N_4 from SnO_2 via ZnO. Thus, the photogenerated electrons and holes are separated and the recombination process is inhibited. The photogenerated electrons are able to react with O_2 to create $O_2^{\bullet-}$, and the holes drift to the surface

DOI: 10.1021/acsomega.8b00471
ACS Omega 2018, 3, 7587−7602

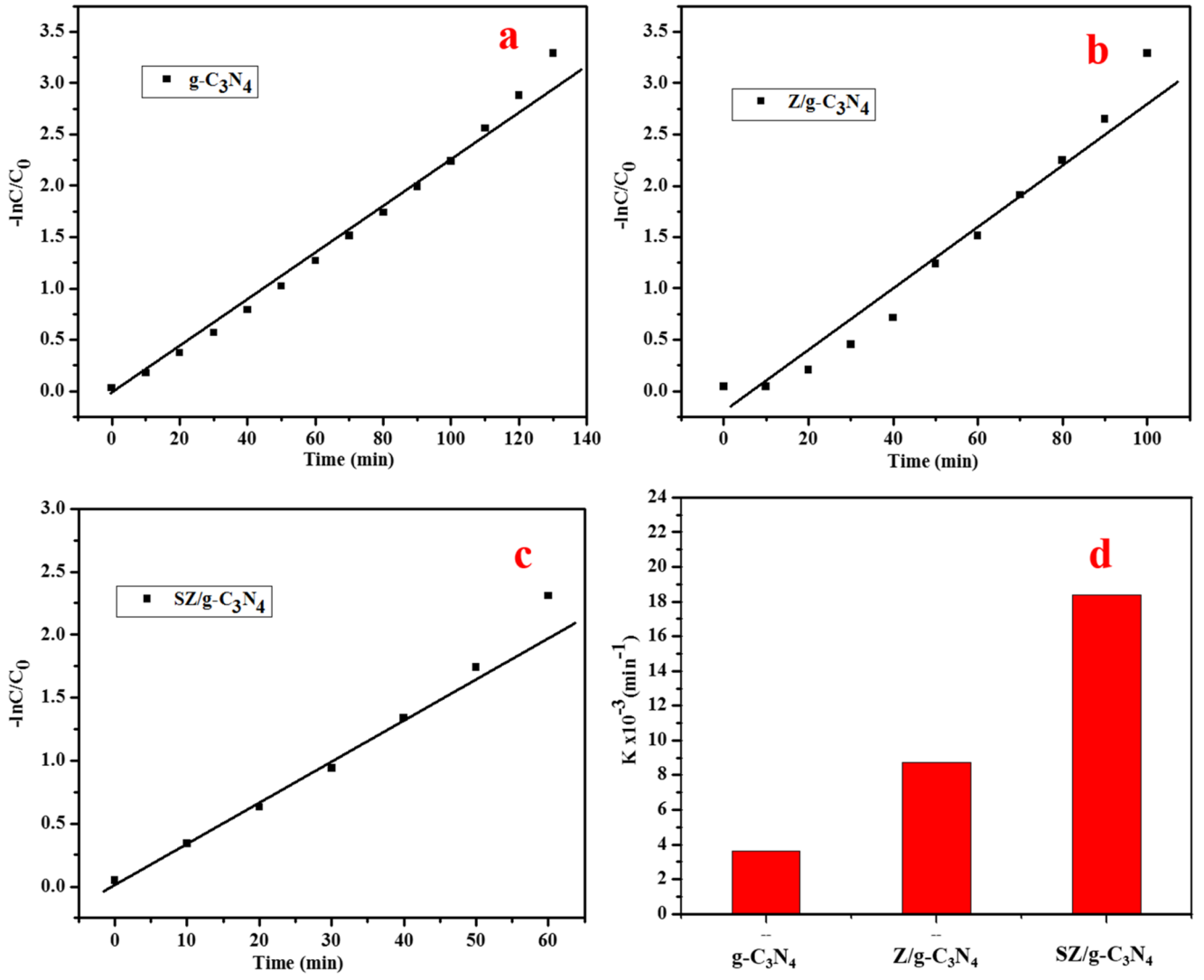

Figure 10. (a−c) Kinetic linear fits and (d) *K* values for the photocatalytic degradation of RhB using different photocatalysts.

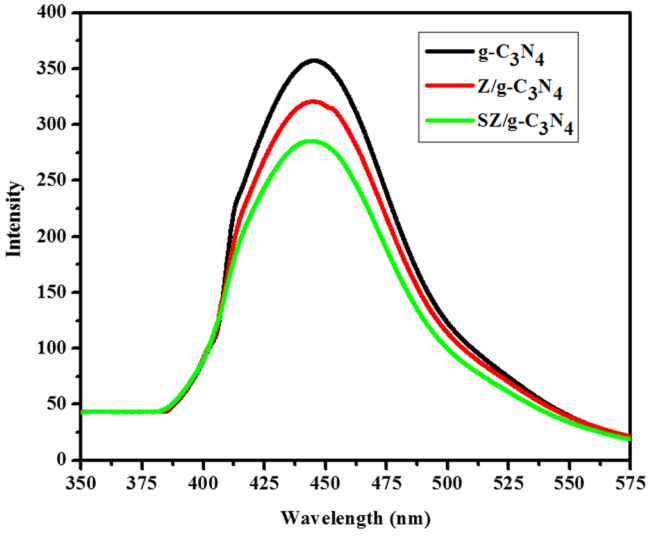

Figure 11. PL spectra of pristine g-C_3N_4, Z/g-C_3N_4, and SZ/g-C_3N_4 catalysts.

of the g-C_3N_4 and react with OH^- or H_2O to produce $^{\bullet}OH$ radicals, as shown in eqs 3−7. Thus, produced $O_2^{\bullet-}$ and $^{\bullet}OH$ radicals are highly oxidative in nature and can oxidize the dye molecules to harmless intermediates and finally mineralizes, as shown in Figure 12.

$$\text{g-}C_3N_4/ZnO/SnO_2 + h\upsilon \rightarrow \text{g-}C_3N_4(e^-, h^+)/ZnO/SnO_2 \quad (3)$$

$$\rightarrow \text{g-}C_3N_4(h^+)/ZnO/SnO_2(e^-) \quad (4)$$

$$e^- + O_2 \rightarrow O_2^{\bullet-} \quad (5)$$

$$h^+ + OH^- \rightarrow {}^{\bullet}OH \quad (6)$$

$$h^+ + H_2O \rightarrow {}^{\bullet}OH + H^+ \quad (7)$$

To test the stability and reusability of the SZ/g-C_3N_4 nanocomposite, repeated degradation cycles under visible-light irradiation were carried out for the photocatalytic degradation of RhB over the SZ/g-C_3N_4 nanocomposite, and Figure S6 shows the recycling test results for the SZ/g-C_3N_4 nanocomposite. There was a minor reduction over the first two cycles of RhB photodegradation, but, after two cycles, the degradation behavior stabilized. These results indicate that the SZ/g-C_3N_4 nanocomposite has great stability and is an

DOI: 10.1021/acsomega.8b00471
ACS Omega 2018, 3, 7587−7602

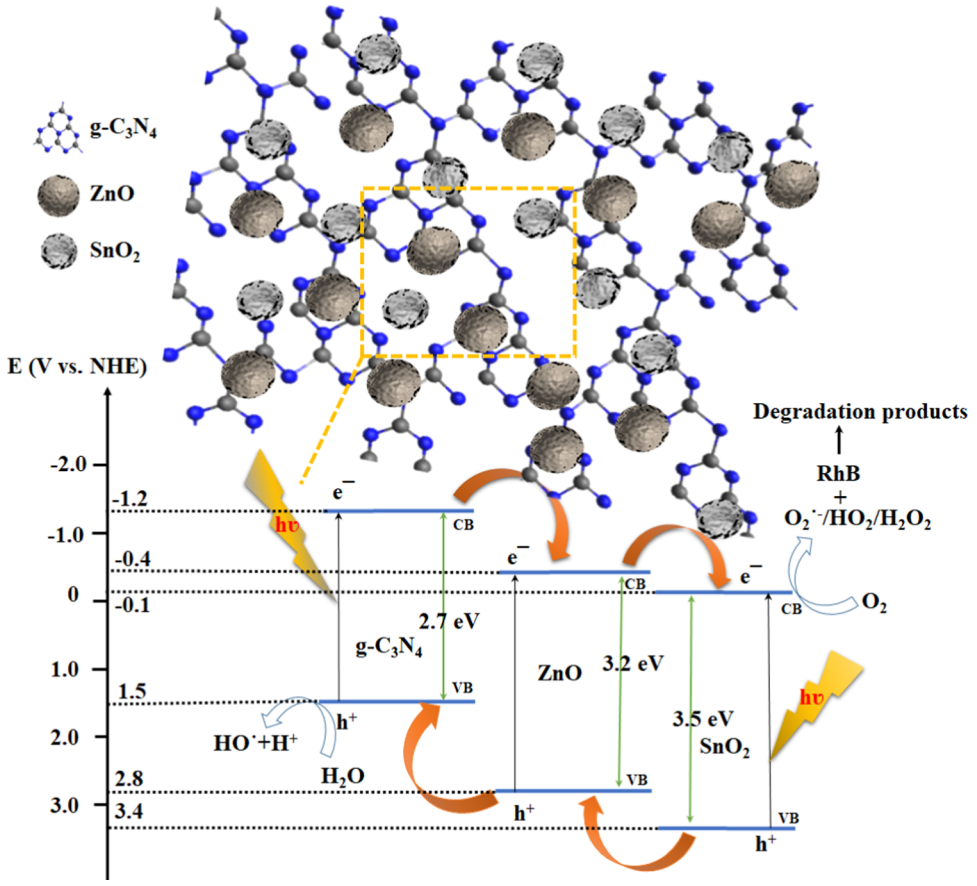

Figure 12. Schematic of a plausible mechanism for photocatalytic degradation over the SZ/g-C_3N_4 heterostructure structure under visible-light irradiation.

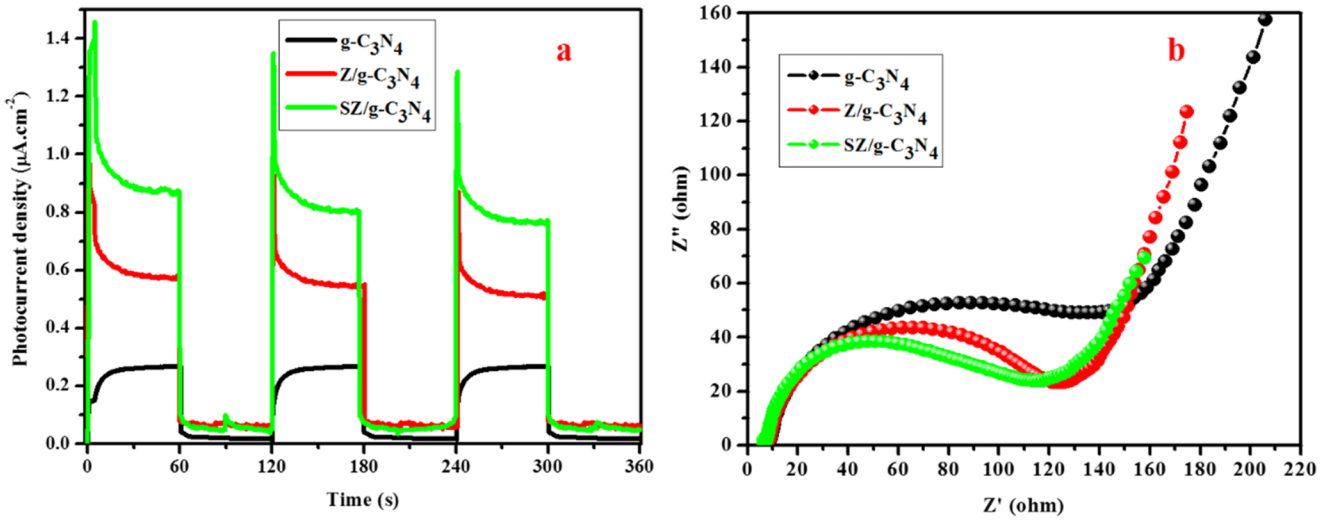

Figure 13. (a) Transient photocurrent studies and (b) EIS spectra of pristine g-C_3N_4, Z/g-C_3N_4, and SZ/g-C_3N_4 catalysts.

encouraging photocatalyst for use in the purification of water resources.

To further understand the separation capability of the photogenerated electron−hole pairs and increased lifetime of the charge carriers, photocurrent (PC) and electrochemical impedance spectroscopy (EIS) measurements were conducted, as shown in Figure 13. During repeated 60 s on−off irradiation cycles, prompt and reproducible current responses were recorded for each electrode. Figure 13a presents the photo-response switching behavior of the different photocatalysts, including g-C_3N_4 and the Z/g-C_3N_4 and SZ/g-C_3N_4 nanocomposites. A slight photocurrent response (0.21 μA cm^{-2}) was observed with the g-C_3N_4 electrode, whereas, for SZ/g-C_3N_4, the photocurrent density reached 0.87 μA cm^{-2}, which is about 4.14 times greater than that of the g-C_3N_4 electrode. Upon illumination, the photocurrent rapidly increased (1.4 μA) and then stabilized at approximately 0.98 μA for the SZ/g-C_3N_4 nanocomposite, drastically decreasing to its initial level when

DOI: 10.1021/acsomega.8b00471
ACS Omega 2018, 3, 7587−7602

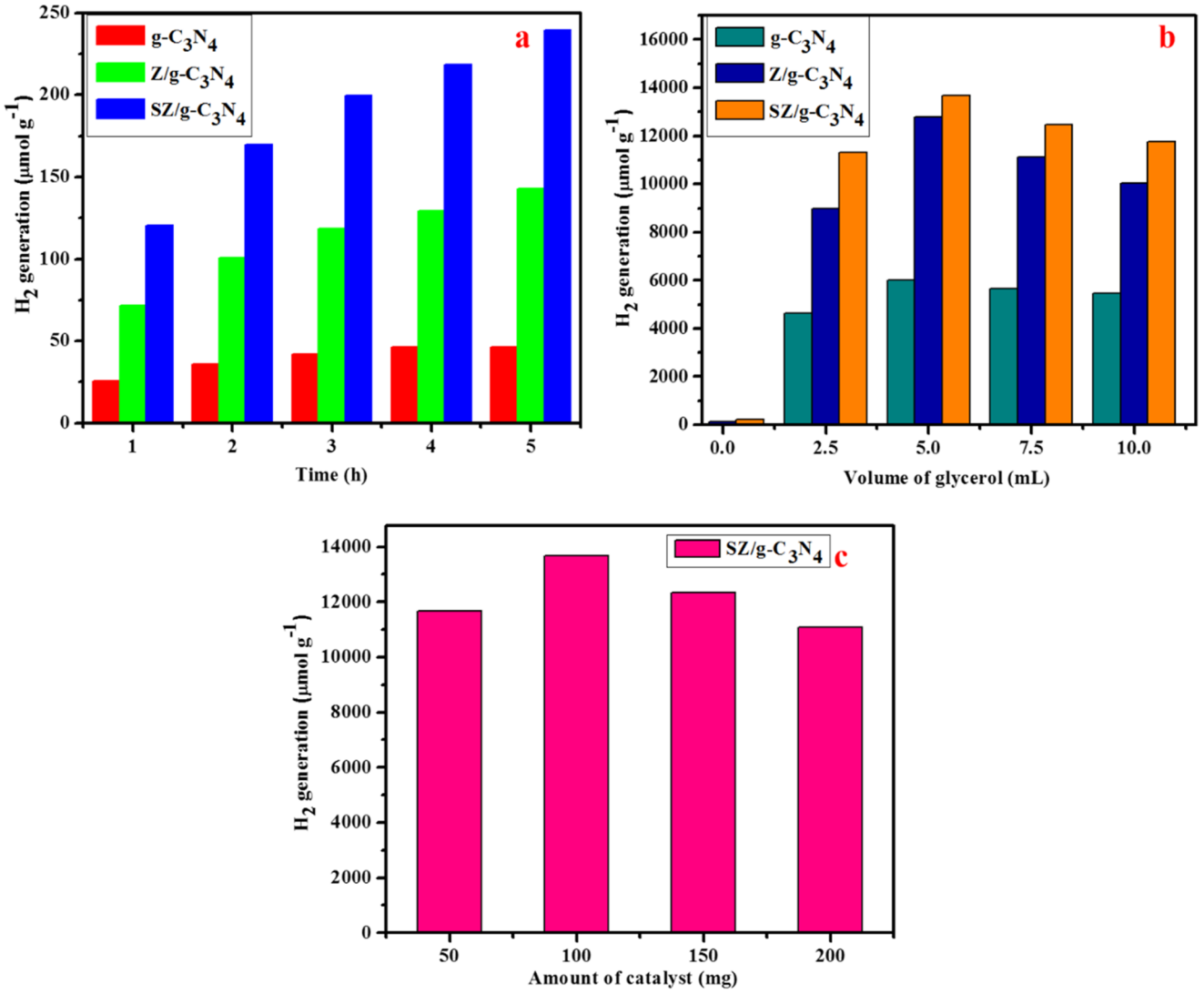

Figure 14. (a) H_2 generation from pure water over different catalysts, (b) effect of the glycerol concentration, and (c) effect of SZ/g-C_3N_4 catalyst amount on the photocatalytic H_2 production under natural and visible-light irradiation (5 h).

the light was turned off. Clearly, the photocurrent of the ternary SZ/g-C_3N_4 nanocomposite is improved remarkably, having a longer life span and more efficient charge separation than other similar materials.[42]

To demonstrate the advantages of the ternary SZ/g-C_3N_4 nanocomposite over the g-C_3N_4 and Z/g-C_3N_4 samples, we also prepared Nyquist plots, which provide powerful evidence to clarify charge-transfer processes at an electrode interface. These plots are shown in Figure 13b. As shown in the Nyquist plots, the SZ/g-C_3N_4 nanocomposite showed the smallest impedance arc radius compared to other samples, which suggests the presence of a lower charge-transfer resistance than that of other samples. This should contribute to a better separation efficiency of the photogenerated electron−hole pairs and improved photocatalytic efficiency of the ternary SZ/g-C_3N_4 nanocomposite. In contrast, the high-frequency arc in the Nyquist plots is related to the reduction in charge transfer, which may be attributed to the double-layer capacitance (C_{dl}) and charge-transfer resistance (R_{ct}) at the contact interface between the electrode and electrolyte solution.

2.2. Photocatalytic H_2 Production. Figure 14a shows hydrogen production from pure water splitting over pristine g-C_3N_4, Z/g-C_3N_4, and SZ/g-C_3N_4 catalysts. The optimum hydrogen production was achieved for SZ/g-C_3N_4 (239.29 μmol g^{-1}). The increase in the photocatalytic activity of SZ/g-C_3N_4 catalyst is due to the presence of tin oxide on the SZ/g-C_3N_4 surface that acts as a co-catalyst. Xiang et al.[43] suggested the importance of heterostructure-type materials for applications in energy conversion systems. This unique structure reduces the charge-carrier transport distance to the surface for redox reactions. Under visible-light irradiation, the lifetime of the electron−hole pairs is increased and the charge carriers are efficiently involved in the redox reactions with adsorbed H^+ ions for H_2 evolution at the catalyst surface. The conditions for optimum photocatalytic hydrogen production over the SZ/g-C_3N_4 catalyst have been attempted. Figure 14b,c shows the effect of the concentration of glycerol and catalyst content on the rate of photocatalytic hydrogen production. To optimize the glycerol concentration, reactions were carried out over the SZ/g-C_3N_4 catalyst using glycerol/water mixtures with various glycerol loadings (Figure 14b). The results show that the glycerol concentration affects the rate of hydrogen production. The optimal concentration of glycerol was found to be 5%, which resulted in a photocatalytic hydrogen production rate of

DOI: 10.1021/acsomega.8b00471
ACS Omega 2018, 3, 7587−7602

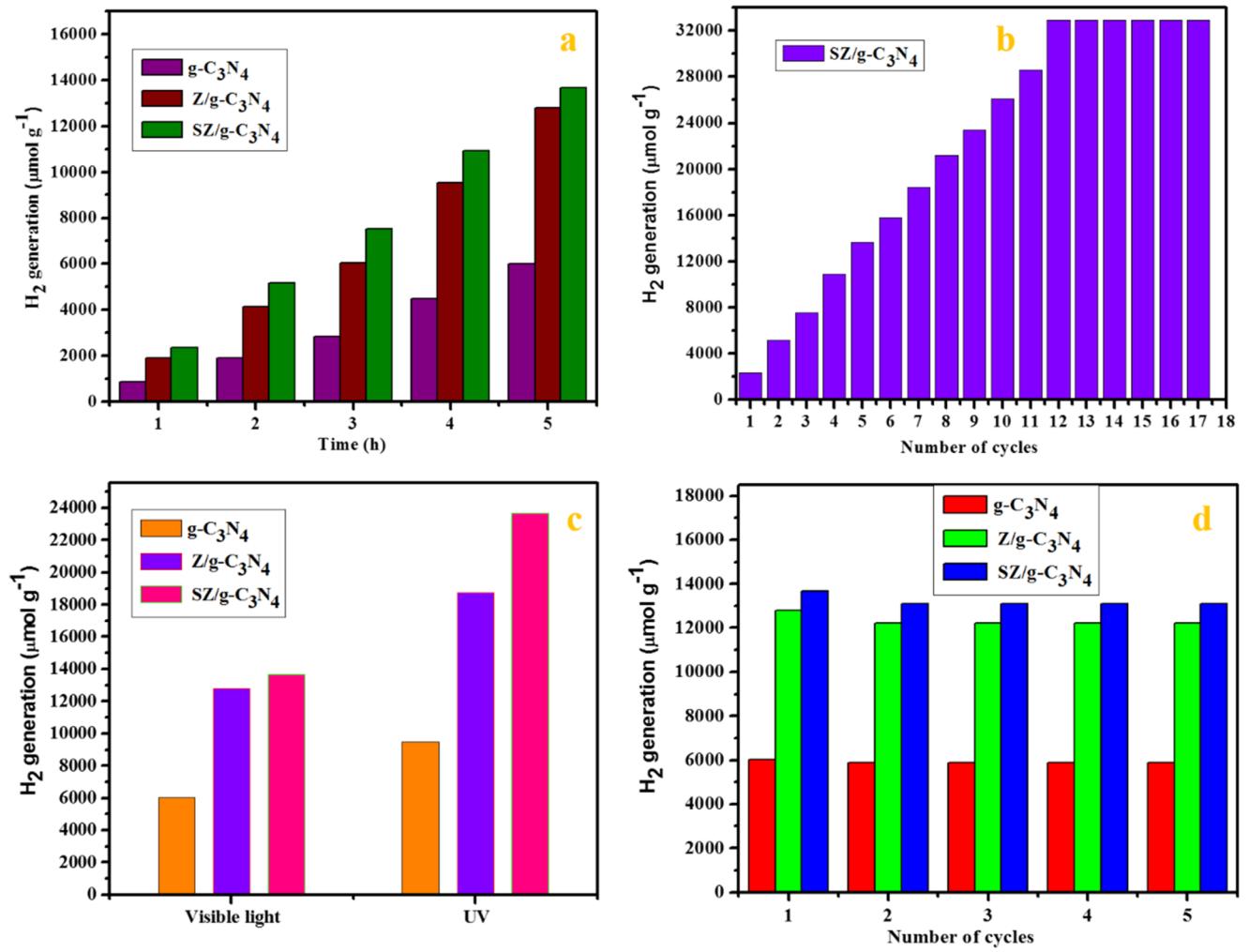

Figure 15. (a) Photocatalytic H_2 production over pristine g-C_3N_4, Z/g-C_3N_4, and SZ/g-C_3N_4 catalysts under visible-light irradiation in 5 mg in 5 vol % glycerol/water solution. (b) Time-on-stream photocatalytic H_2 production activity over the SZ/g-C_3N_4 catalyst under visible-light irradiation in 5 vol % glycerol/water solution. (c) Hydrogen evolution rates of SZ/g-C_3N_4 catalyst under visible- and UV-light irradiation for 5 h (UV light source: 4 W lamp; wavelength, 254 nm; and light intensity, 340 mW cm^{-2}; visible source, 300 W Xe lamp; light intensity, 50 mW cm^{-2}). (d) Recyclability of SZ/g-C_3N_4 catalyst for photocatalytic H_2 production activity under visible-light irradiation in 5 mg in 5 vol % glycerol/water solution for 5 h.

13 673.61 μmol g^{-1}. In detail, the photocatalytic hydrogen production rate increases with increasing initial glycerol concentration up to 5%. Above 5% glycerol concentration, there is no increase in H_2 production. This is because, at higher concentrations, saturation of the photocatalyst surface occurs, and there is no further increase in H_2 production. In addition, the amount of the catalyst in the reaction system also has a notable effect on the photocatalytic hydrogen production rate (Figure 14c). The SZ/g-C_3N_4 catalyst was added at loadings of 50, 100, 150, and 200 mg L^{-1} in a 5% glycerol/water solution. The optimum hydrogen production rate of 13 673.61 μmol g^{-1} was observed with a catalyst loading of 100 mg L^{-1}. With increasing catalyst loading, the hydrogen production increased. However, a higher catalyst loading is disadvantageous for photocatalytic hydrogen production because the higher amounts of catalyst make the solution turbid, which inhibits the absorption of incident light by hindering light transmission. After several hours, the partial pressure of H_2 in the reactor increased, which resulted in increased H_2 solubility in the solution; thus, the volume of the reactor became insufficient to accommodate the large amount of H_2 generated by the water-splitting reaction.

The photocatalytic activities for hydrogen production from a 5% aqueous glycerol solution as a function of time over different photocatalysts (i.e., pristine g-C_3N_4, Z/g-C_3N_4, and SZ/g-C_3N_4) are shown in Figure 15a. Among these, the SZ/g-C_3N_4 catalyst exhibited the highest activity. The improved rate of H_2 production could have resulted from the favorable properties of the heterostructure-type SnO_2−ZnO nanoparticles, which achieve a higher energy density because of the higher content of active species on the surface of g-C_3N_4. As demonstrated by the EIS results, the g-C_3N_4 nanosheets, which are readily dispersed and form strong interactions with the SnO_2−ZnO nanoparticles, have high electrical conductivity, which leads to a remarkable separation of the photogenerated charge carriers and enhances the surface shuttling properties. The photocatalytic activity increases in the order g-C_3N_4 < Z/g-C_3N_4 < SZ/g-C_3N_4. The optimum hydrogen production of 13 673.61 μmol g^{-1} was observed on SZ/g-C_3N_4 after 5 h irradiation, and this is about 2.27 times higher than that of pristine g-C_3N_4, i.e., 6017.72 μmol g^{-1}, and 1.06 times higher than that of Z/g-C_3N_4, i.e., 12 785.54 μmol g^{-1}. Under visible-light irradiation, charge carriers are produced in g-C_3N_4 and are transferred to the conduction band of ZnO and SnO_2. ZnO and

DOI: 10.1021/acsomega.8b00471
ACS Omega 2018, 3, 7587−7602

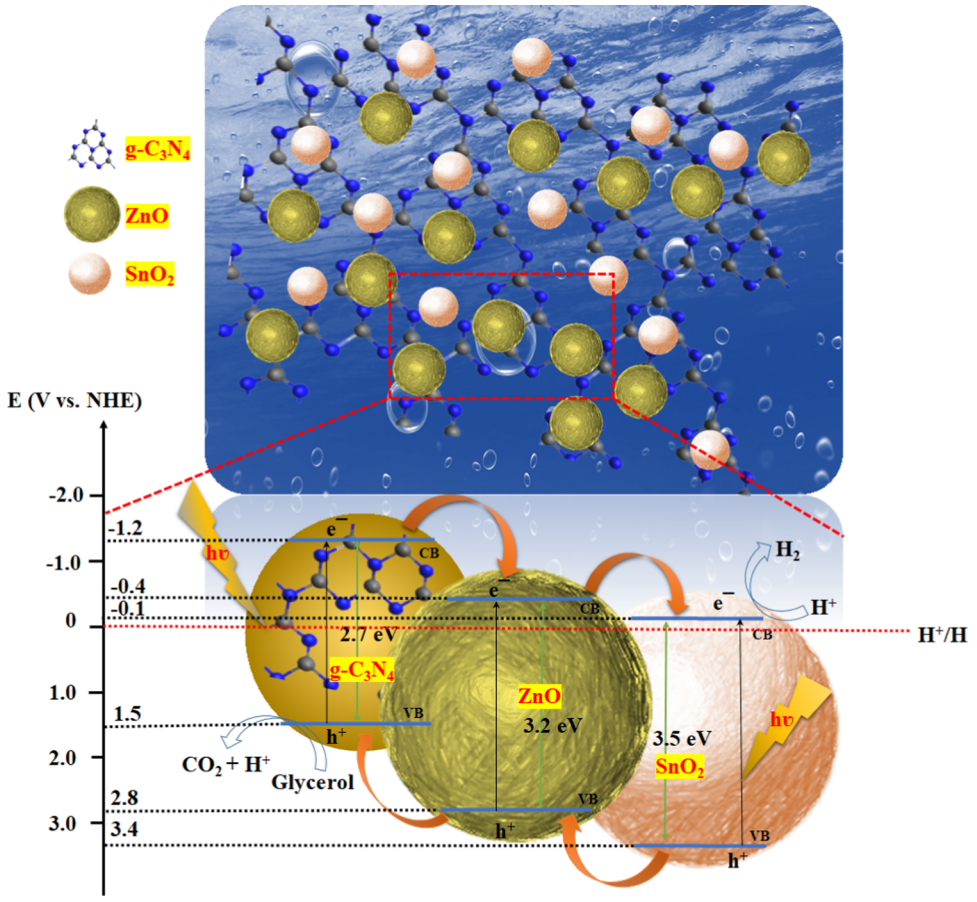

Figure 16. Schematic illustration of a plausible mechanism for photocatalytic H_2 production over SZ/g-C_3N_4 catalyst under visible-light irradiation.

SnO_2 act as co-catalysts and trap these electrons. Thus, the lifetime of the electron−hole pairs is increased and the charge carriers can carry out redox reactions with adsorbed H^+ ions for H_2 evolution at the catalyst surface. The factors responsible for the improved activity are the enhanced optical absorption and increased lifetime of the charge carriers. The highly dispersed ZnO−SnO_2 particles on the surface of g-C_3N_4 act as a co-catalyst and contribute to the increased lifetime of the charge carriers. Hence, the enhanced activity is ascribed to the synergistic effect of the increased optical absorption and the improved lifetime of the charge carriers in the system. The improved photocatalytic activity of g-C_3N_4 with deposited tin and zinc oxides compared to pristine g-C_3N_4 may be ascribed to the following reasons: (i) surface impurities formed by tin and zinc oxides increase the visible absorption by decreasing the band gap of pristine g-C_3N_4, as shown by UV−vis DRS measurements[44−46] and (ii) increase in the lifetime of the charge carriers.

Figure 15b shows the time-on-stream activity over the SZ/g-C_3N_4 catalyst. As shown by the data, the activity increases linearly up to 11 h and then stabilizes. This is because the capacity of the photoreactor might have become inadequate for further production of hydrogen after 11 h and some of the formed H_2 molecules might have occupied the active sites on the photocatalyst surface. The decrease in the rate of hydrogen production with time may also be due to the pressure developed by the produced hydrogen during the reaction. Also, the volume of the reactor might become insufficient to accommodate the further produced hydrogen. Thus, for these reasons, the production of hydrogen is hindered.

Figure 15c shows the rate of photocatalytic H_2 production over different catalysts under visible-light and UV-light irradiation. The SZ/g-C_3N_4 catalyst demonstrated a higher rate of H_2 production under UV light irradiation compared to visible-light irradiation because of the greater absorption capability of the composite. Additionally, stability tests were performed using three consecutive photocatalytic activity experiments, where each reaction was performed for 5 h irradiation with repeated gas evacuation and N_2 purging each cycle. Figure 15d shows the results of recycling experiment over pristine g-C_3N_4, Z/g-C_3N_4, and SZ/g-C_3N_4 catalysts. Identical amounts of H_2 were produced in all five successive experiments. When the gases were removed, the activity was found to be maintained up to five cycles. This result indicates that the activity is sustainable for even longer periods of exposure to visible light. Moreover, to check the changes in the morphology and crystallinity after the recycling experiments, HRTEM and XRD measurements of the used SZ/g-C_3N_4 catalyst were performed after the completion of the continuous photocatalytic experiments, and the results are shown in Figure S7. The morphology and structural analyses show that the heterostructure of SnO_2−ZnO nanoparticles anchored on the surface of g-C_3N_4 was stable even after five cycles of photocatalytic hydrogen evolution.

2.3. Structure−Activity Correlation. On the basis of the analytical results, the impregnation of tin and zinc oxides on the surface of g-C_3N_4 resulted in a fine dispersion of tightly bound SnO_2 and ZnO species over the surface of g-C_3N_4. The possible photoexcitation and charge-transfer processes that take place in the SZ/g-C_3N_4 catalysts are illustrated in Figure 16. In the

DOI: 10.1021/acsomega.8b00471
ACS Omega 2018, 3, 7587−7602

ternary SZ/g-C_3N_4 nanocomposite, since the conduction band potential of g-C_3N_4 (−1.2 eV vs NHE)[47] is more negative than the conduction band potentials of ZnO (−0.4 eV vs NHE)[48] and SnO_2 (−0.1 eV vs NHE),[49] the transfer of photogenerated electrons from g-C_3N_4 to ZnO and SnO_2 is thermodynamically feasible. At the same time, due to the more positive nature of VB potentials of ZnO and SnO_2, the hole transfer takes place from SnO_2 and ZnO to g-C_3N_4 opposite to the direction of electrons transfer. This results in the accumulation of electrons and holes on different semiconductor photocatalysts, which results in the reduction of recombination process. As the catalyst is exposed to visible light, g-C_3N_4 absorbs visible light and produces e^- and h^+ in the CB and VB, respectively.[50] Electrons are then injected into the conduction band of SnO_2 via ZnO. To increase the activity, the recombination of e^- and h^+ should be diminished. The finely dispersed SnO_2 and ZnO species acts as e^- receptors and reduce the recombination of charge carriers. The electrons stored in the conduction band of SnO_2 are transferred to H^+ ions and produce H_2. Meanwhile, the holes in the valence band of g-C_3N_4 are consumed by the sacrificial agent, which further prevents recombination. Subsequently, the recombination of photogenerated charge carriers is suppressed and H_2 production is boosted.

2.4. Reason for the Enhanced Catalytic Activity of the SZ/g-C_3N_4 Nanocomposite. On the basis of the reported analytical results, the following factors are responsible for improving the photocatalytic activity of the SZ/g-C_3N_4 nanocomposite for the degradation of the anionic dye RhB and improved H_2 production under visible-light irradiation: (i) In situ synthesized SnO_2−ZnO/g-C_3N_4 demonstrates good interfacial contact strength that results in a synergistic effect between g-C_3N_4 and SnO_2−ZnO nanoparticles for fast electron transfer. HRTEM images of SZ/g-C_3N_4 nanocomposite reveal small (ca. 5 nm) SnO_2−ZnO nanoparticles randomly distributed on the surface of the g-C_3N_4 nanosheets; (ii) the band gap narrowing of the SZ/g-C_3N_4 nanocomposite increased the speed of electron transfer for the degradation reaction; (iii) the photocurrent and EIS results revealed a high separation efficiency and diminished electron−hole pair recombination; and (iv) the high specific surface area and active sites of the SZ/g-C_3N_4 nanocomposite.

3. CONCLUSIONS

We have successfully synthesized a new type of SZ/g-C_3N_4 nanocomposite photocatalyst via a simple co-pyrolysis method. The photocatalytic degradation of a model pollutant and H_2 production indicate the improved visible-light-driven photocatalytic performance of the ternary SZ/g-C_3N_4 nanocomposite. The separation ratio of the photogenerated electron−hole pairs has been greatly enhanced because of the use of ZnO and SnO_2 quantum dots that decorate the g-C_3N_4 nanosheets, where g-C_3N_4 acts as an outstanding electron transporter and support material. The recycling results for the SZ/g-C_3N_4 catalyst indicate its acceptable photocatalytic stability. In view of the high photoactivity and recycling stability of the SZ/g-C_3N_4 nanocomposite, it has possible applications in the photocatalytic degradation of other organic pollutants in wastewater and production of H_2.

4. EXPERIMENTAL SECTION

4.1. Materials. Thiourea was purchased from Junsei Chemical Co., Ltd. Zinc acetate dihydrate and tin (II) chloride dihydrate were purchased from Sigma-Aldrich.

4.2. Synthesis of g-C_3N_4 Photocatalyst. The synthetic procedure for the preparation of g-C_3N_4 is the same as previously reported.[25] In detail, thiourea was calcined at 550 °C for 6 h at a heating rate of 10 °C min^{-1}, yielding a yellow product. This product was washed with ethanol and dried at 90 °C for 3 h in a muffle furnace.

4.3. Synthesis of ZnO/g-C_3N_4 and SnO_2−ZnO/g-C_3N_4 Photocatalysts. For the preparation of ZnO/g-C_3N_4, a certain amount of thiourea and zinc acetate dihydrate precursors were ground in an agate mortar and transferred to a ceramic crucible, which was maintained at 550 °C for 6 h at a heating rate of 10 °C min^{-1} to yield ZnO/g-C_3N_4. Finally, the precipitates were washed with ethanol and dried at 90 °C for 3 h in a muffle furnace. A similar procedure followed with the addition of tin precursor to form SnO_2−ZnO/g-C_3N_4. Hereafter, ZnO/g-C_3N_4 is denoted "Z/g-C_3N_4" and SnO_2−ZnO/g-C_3N_4 is denoted "SZ/g-C_3N_4".

4.4. Characterization. All of the as-prepared photocatalysts were characterized by X-ray diffraction (Shimadzu 6100 X-ray diffractometer) using Cu Kα radiation. The morphologies of the as-prepared photocatalysts were characterized by high-resolution transmission electron microscopy (HRTEM), and the HRTEM images were obtained using a Tecnai G2 F20 S-Twin TEM at an accelerating voltage of 300 kV. Scanning electron microscopy (SEM; Hitachi S-4100) and energy-dispersive X-ray spectroscopy were used to investigate the composition and structure of the photocatalyst. The infrared (IR) spectra were recorded at a resolution of 4 cm^{-1} in the spectral range 400−4000 cm^{-1} using 32 scans on an Avatar 370 Fourier transform (FT)-IR spectrometer. UV−vis spectra of the photocatalysts were obtained on a UV−vis spectrophotometer (Cary 5000 UV−vis−NIR, spectrophotometer). High-resolution X-ray photoelectron spectroscopy (XPS) measurements were carried out using a Thermo Scientific instrument and Mg Kα X-rays for surface analysis. The nitrogen adsorption−desorption isotherms were analyzed using a Micromeritics ASAP 2420 surface area analyzer at liquid nitrogen temperature. Prior to gas adsorption, all photocatalysts were degassed for 2 h at 160 °C. Photocurrent (PC) response measurements were performed using a Biologic SP-200 electrochemical workstation with a standard three-electrode cell at room temperature. Electrochemical impedance spectroscopy (EIS) was carried out using a potentiostat with a sinusoidal perturbation voltage of 2 mV and the frequency range of 0.01 Hz to 1 MHz. The Sn and Zn metal contents in the prepared samples were analyzed by inductively coupled plasma-optical emission spectroscopy (ICP-OES) using the Varian 700-ES model.

4.5. Photocatalytic Degradation of the RhB Dye and H_2 Production. The photodegradation of RhB was performed at room temperature in a photochemical reactor containing 40 mg of photocatalyst and 100 mL of RhB solution. To obtain adsorption−desorption equilibrium, the photocatalyst was maintained in the dark for 10 min after adsorption−desorption balance had been achieved. To check that the photocatalytic activity arose from the photocatalyst only, we carried out blank experiments without a photocatalyst under visible-light irradiation (photolysis). A 300 W xenon lamp (Max 303, 1

DOI: 10.1021/acsomega.8b00471
ACS Omega 2018, 3, 7587−7602

sun light) was used as the light source (light intensity, 50 mW cm^{-2}), which was located approximately 6 cm to one side of the solution. A glass filter was used to remove the UV light and IR light (Hoya, 77 mm, wavelength of UV < 390 nm and IR > 700 nm). At 10 min intervals, the photocatalysts were separated by centrifugation at 5000 rpm for 10 min and the light absorption of a clear solution of the different photocatalysts was recorded using an UV−vis spectrophotometer (Cary 5000 UV−vis−NIR spectrophotometer).

Photocatalytic H_2 production was measured using a lab-made experimental setup. A 300 W xenon lamp (Max 303 model) (λ > 400 nm) with an intensity of 50 mW cm^{-2} was used as the light source and placed parallel to the reactor. In a typical photocatalytic H_2 production trial, 5 mg of photocatalyst was dispersed in 50 mL of 5% aqueous glycerol solution with vigorous stirring and the stirring was continuous so that uniform irradiation of the photocatalyst suspension was achieved throughout the tests. Prior to irradiation, the system was subjected to vacuum to remove dissolved oxygen from the solution. The solution was then purged with N_2 gas. The generated gas was collected each hour, and the hydrogen content was determined by gas chromatography (6500GC System, YL Instruments, with thermal conductivity detector). Helium was used as the carrier gas.

■ ASSOCIATED CONTENT

Supporting Information

The Supporting Information is available free of charge on the ACS Publications website at DOI: 10.1021/acsomega.8b00471.

HRTEM images; SEM image; SEM-EDX spectra; ICP-OES analysis; UV−vis absorption spectra; recycling test; XRD pattern (Figures S1−S7) (PDF)

■ AUTHOR INFORMATION

Corresponding Authors

*E-mail: drprabu@ynu.ac.kr. Mobile: +82-(0)53-810-2452. Fax: +82-53-810-4627 (S.V.P.V.).
*E-mail: jshim@ynu.ac.kr (J.S.).

ORCID

S. V. Prabhakar Vattikuti: 0000-0002-9009-5466

Notes

The authors declare no competing financial interest.

■ ACKNOWLEDGMENTS

This study was supported by the National Research Foundation of Korea (NRF) and funded by the Ministry of Science, ICT, and Future Planning (2017R1A2B1004860). It was also supported by a National Research Foundation of Korea (NRF) grant funded by the Korean government (2017R1A4A1015581).

■ REFERENCES

(1) Christoforidis, K. C.; Fornasiero, P. Photocatalytic Hydrogen Production: A Rift into the Future Energy Supply. *ChemCatChem* **2017**, *9*, 1523−1544.

(2) Mao, S. S.; Shen, S.; Guo, L. Nanomaterials for renewable hydrogen production, storage and utilization. *Prog. Nat. Sci.: Mater. Int.* **2012**, *22*, 522−534.

(3) Tee, S. Y.; Win, K. Y.; Teo, W. S.; Koh, L.; Liu, S.; Teng, C. P.; Han, M. Y. Progress in Energy-Driven Water Splitting. *Adv. Sci.* **2017**, *4*, No. 1600337.

(4) Chiarello, G. L.; Dozzi, M. V.; Selli, E. TiO_2-based materials for photocatalytic hydrogen production. *J. Energy Chem.* **2017**, *26*, 250−258.

(5) Kim, J. S.; Oh, J. W.; Woo, S. I. Improvement of the photocatalytic hydrogen production rate of g-C_3N_4 following the elimination of defects on the surface. *Catal. Today* **2017**, *293*−*294*, 8−14.

(6) Tay, Q.; Kanhere, P.; Ng, C. F.; Chen, S.; Chakraborty, S.; Huan, A. C. H.; Sum, T. C.; Ahuja, R.; Chen, Z. Defect Engineered g-C_3N_4 for Efficient Visible Light Photocatalytic Hydrogen Production. *Chem. Mater.* **2015**, *27*, 4930−4933.

(7) Peng, T.-y.; Lv, H.-j.; Zeng, P.; Zhang, X.-h. Preparation of ZnO Nanoparticles and Photocatalytic H_2 Production Activity from Different Sacrificial Reagent Solutions. *Chin. J. Chem. Phys.* **2011**, *24*, 464−470.

(8) Pirhashemi, M.; Habibi-Yangjeh, A.; Pouran, S. R. Review on the criteria anticipated for the fabrication of highly efficient ZnO-based visible-light-driven photocatalysts. *J. Ind. Eng. Chem.* **2018**, 1−25.

(9) Charvin, P.; Abanades, S.; Lemont, F.; Flamant, G. Experimental study of SnO_2/SnO/Sn thermochemical systems for solar production of hydrogen. *AIChE J.* **2008**, *54*, 2759−2767.

(10) Zhang, H.; Hu, C.; Chen, S.; Zhang, K.; Wang, X. Synthesis of SnO_2 Nanostructures and Their Application for Hydrogen Evolution Reaction. *Catal. Lett.* **2012**, *142*, 809−815.

(11) Hai, X.; Zhou, W.; Chang, K.; Pang, H.; Liu, H.; Shi, L.; Ichihara, H.; Ye, J. Engineering the crystallinity of MoS_2 monolayers for highly efficient solar hydrogen production. *J. Mater. Chem. A* **2017**, *5*, 8591−8598.

(12) Iqbal, W.; Qiu, B.; Lei, J.; Wang, L.; Zhang, J.; Anpo, M. One-step large-scale highly active g-C_3N_4 nanosheets for efficient sunlight-driven photocatalytic hydrogen production. *Dalton Trans.* **2017**, *46*, 10678−10684.

(13) Mousavi, M.; Habibi-Yangjeh, A.; Pouran, S. R. Review on magnetically separable graphitic carbon nitride-based nanocomposites as promising visible-light-driven photocatalysts. *J. Mater. Sci.: Mater. Electron.* **2018**, *29*, 1719−1747.

(14) Liu, Y.; Shen, C.; Jiang, N.; Zhao, Z.; Zhou, X.; Zhao, S.; Xu, A. g-C_3N_4 Hydrogen-Bonding Viologen for Significantly Enhanced Visible-Light Photocatalytic H_2 Evolution. *ACS Catal.* **2017**, *7*, 8228−8234.

(15) Zhang, G.; Lan, Z.; Lin, L.; Lin, S.; Wang, X. Overall water splitting by Pt/g-C_3N_4 photocatalysts without using sacrificial agents. *Chem. Sci.* **2016**, *7*, 3062−3066.

(16) Akhundi, A.; Habibi-Yangjeh, A. Graphitic carbon nitride nanosheets decorated with $CuCr_2O_4$ nanoparticles: Novel photocatalysts with high performances in visible light degradation of water pollutants. *J. Colloid Interface Sci.* **2017**, *504*, 697−710.

(17) Samanta, S.; Martha, S.; Parid, K. Facile Synthesis of Au/g-C_3N_4 Nanocomposites: An Inorganic/Organic Hybrid Plasmonic Photocatalyst with Enhanced Hydrogen Gas Evolution Under Visible-Light Irradiation. *ChemCatChem* **2014**, *6*, 1453−1462.

(18) Nagajyothi, P. C.; Pandurangan, M.; Vattikuti, S. V. P.; Tettey, C. O.; Sreekanth, T. V. M.; Shim, J. Enhanced photocatalytic activity of Ag/g-C_3N_4 composite. *Sep. Purif. Technol.* **2017**, *188*, 228−237.

(19) Chen, X.; Zhou, B.; Yang, S.; Wu, H.; Wu, Y.; Wu, L.; Pan, J.; Xiong, X. In situ construction of an SnO_2/g-C_3N_4 heterojunction for enhanced visible-light photocatalytic activity. *RSC Adv.* **2015**, *5*, 68953−68963.

(20) Liu, C.; Li, C.; Fu, X.; Raziq, F.; Qu, Y.; Jing, L. Synthesis of silicate-bridged ZnO/g-C_3N_4 nanocomposites as efficient photocatalysts and its mechanism. *RSC Adv.* **2015**, *5*, 37275−37280.

(21) Chidhambaram, N.; Ravichandran, K. Fabrication of ZnO/g-C_3N_4 nanocomposites for enhanced visible light driven photocatalytic activity. *Mater. Res. Exp.* **2018**, *4*, No. 075037.

(22) Chai, B.; Peng, T.; Mao, J.; Lia, K.; Zan, L. Graphitic carbon nitride (g-C_3N_4)−Pt-TiO_2 nanocomposite as an efficient photocatalyst for hydrogen production under visible light irradiation. *Phys. Chem. Chem. Phys.* **2012**, *14*, 16745−16752.

DOI: 10.1021/acsomega.8b00471
ACS Omega 2018, 3, 7587−7602

(23) Ji, H.; Fan, Y.; Yan, J.; Xu, Y.; She, X.; Gu, J.; Fei, T.; Xu, H.; Li, H. Construction of SnO_2/graphene-like g-C_3N_4 with enhanced visible light photocatalytic activity. *RSC Adv.* **2017**, *7*, 36101−36111.
(24) Shen, H.; Zhao, X.; Duan, L.; Liu, R.; Li, H. Enhanced visible light photocatalytic activity in SnO_2@g-C_3N_4 core-shell structures. *Mater. Sci. Eng., B* **2017**, *218*, 23−30.
(25) Vattikuti, S. V. P.; Byon, C. Hydrothermally synthesized ternary heterostructured MoS_2/Al_2O_3/g-C_3N_4 photocatalyst. *Mater. Res. Bull.* **2017**, *96*, 233−245.
(26) Zhou, J.; Zhang, M.; Zhu, Y. Preparation of visible light-driven g-C_3N_4@ZnO hybrid photocatalyst via mechanochemistry. *Phys. Chem. Chem. Phys.* **2014**, *16*, 17627−17633.
(27) Ansari, S. A.; Khan, M. M.; Ansari, M. O.; Lee, J.; Cho, M. H. Biogenic Synthesis, Photocatalytic, and Photoelectrochemical Performance of Ag−ZnO Nanocomposite. *J. Phys. Chem. C* **2013**, *117*, 27023−27030.
(28) Ansari, S. A.; Khan, M. M.; Kalathil, S.; Nisar, A.; Lee, J.; Cho, M. H. Oxygen vacancy induced band gap narrowing of ZnO nanostructures by an electrochemically active biofilm. *Nanoscale* **2013**, *5*, 9238−9246.
(29) Hu, D.; Han, B.; Deng, S.; Feng, Z.; Wang, Y.; Popovic, J.; Nuskol, M.; Wang, Y.; Djerdj, I. Novel Mixed Phase SnO_2 Nanorods Assembled with SnO_2 Nanocrystals for Enhancing Gas-Sensing Performance toward Isopropanol Gas. *J. Phys. Chem. C* **2014**, *118*, 9832−9840.
(30) Zada, A.; Humayun, M.; Raziq, F.; Zhang, X.; Qu, Y.; Bai, L.; Qin, C.; Jing, L.; Fu, H. Exceptional Visible-Light-Driven Cocatalyst-Free Photocatalytic Activity of g-C_3N_4 by Well Designed Nanocomposites with Plasmonic Au and SnO_2. *Adv. Energy Mater.* **2016**, *6*, No. 1601190.
(31) Wang, X.; Hong, M.; Zhang, F.; Zhuang, Z.; Yu, Y. Recyclable Nanoscale Zero Valent Iron Doped g-C_3N_4/MoS_2 for Efficient Photocatalysis of RhB and Cr(VI) Driven by Visible Light. *ACS Sustainable Chem. Eng.* **2016**, *4*, 4055−4063.
(32) Akhundi, A.; Habibi-Yangjeh, A. Ternary g-C_3N_4/ZnO/AgCl nanocomposites: Synergistic collaboration on visible-light-driven activity in photodegradation of an organic pollutant. *Appl. Surf. Sci.* **2015**, *358*, 261−269.
(33) Mousavi, M.; Habibi-Yangjeh, A. Magnetically separable ternary g-C_3N_4/Fe_3O_4/BiOI nanocomposites: Novel visible-light-driven photocatalysts based on graphitic carbon nitride. *J. Colloid Interface Sci.* **2016**, *465*, 83−92.
(34) Mousavi, M.; Habibi-Yangjeh, A. Integration of $NiWO_4$ and Fe_3O_4 with graphitic carbon nitride to fabricate novel magnetically recoverable visible-light-driven photocatalysts. *J. Mater. Sci.* **2018**, *53*, 9046−9063.
(35) Cao, S.; Yu, J. g-C_3N_4-Based Photocatalysts for Hydrogen Generation. *J. Phys. Chem. Lett.* **2014**, *5*, 2101−2107.
(36) Lin, Y.; Hsueh, Y.; Lee, P.; Wang, C.; Wu, J.; Perng, T.; Shih, H. C. Fabrication of tin dioxide nanowires with ultrahigh gas sensitivity by atomic layer deposition of platinum. *J. Mater. Chem.* **2011**, *21*, 10552−10558.
(37) Hu, K.; Li, Z.; Chen, S.; Bian, J.; Qu, Y.; Tang, J.; Jing, L. Synthesis of Silicate-Bridged Heterojunctional SnO_2/$BiVO_4$ Nanoplates as Efficient Photocatalysts to Convert CO_2 and Degrade 2,4-Dichlorophenol. *Part. Part. Syst. Charact.* **2018**, *35*, No. 1700320.
(38) Chuang, P.; Wu, K.; Yeh, T.; Teng, H. Extending the π-Conjugation of g-C_3N_4 by Incorporating Aromatic Carbon for Photocatalytic H_2 Evolution from Aqueous Solution. *ACS Sustainable Chem. Eng.* **2016**, *4*, 5989−5997.
(39) Dong, Y.; Chen, Y.; Jiang, P.; Wang, G.; Wu, X.; Wu, R. A novel g-C_3N_4 based photocathode for photoelectrochemical hydrogen evolution. *RSC Adv.* **2016**, *6*, 7465−7473.
(40) Kumar, R.; Barakat, M. A.; Alseroury, F. A. Oxidized g-C_3N_4/polyaniline nanofiber composite for the selective removal of hexavalent chromium. *Sci. Rep.* **2017**, *7*, No. 12850.
(41) Thangavel, S.; Venugopal, G.; Kim, S. J. Enhanced photocatalytic efficacy of organic dyes using β-tin tungstate-reduced graphene oxide nanocomposites. *Mater. Chem. Phys.* **2014**, *145*, 108−115.
(42) Faraji, M.; Mohaghegh, N.; Abedini, A. Ternary composite of TiO_2 nanotubes/Ti plates modified by g-C_3N_4 and SnO_2 with enhanced photocatalytic activity for enhancing antibacterial and photocatalytic activity. *J. Photochem. Photobiol., B* **2018**, *178*, 124−132.
(43) Xiang, Q.; Yu, J.; Jaronie, M. Preparation and Enhanced Visible-Light Photocatalytic H_2-Production Activity of Graphene/C_3N_4 Composites. *J. Phys. Chem. C* **2011**, *115*, 7355−7363.
(44) Park, T. J.; Pawar, R. C.; Kang, S.; Lee, C. S. Ultra-thin coating of g-C_3N_4 on an aligned ZnO nanorod film for rapid charge separation and improved photodegradation performance. *RSC Adv.* **2016**, *6*, 89944−89952.
(45) Ansari, S. A.; Cho, M. H. Growth of three-dimensional flower-like SnS_2 on g-C_3N_4 sheets as an efficient visible-light photocatalyst, photoelectrode, and electrochemical supercapacitance material. *Sustainable Energy Fuels* **2017**, *1*, 510−519.
(46) Vattikuti, S. V. P.; Police, A. K. R.; Shim, J.; Byon, C. In situ fabrication of the Bi_2O_3−V_2O_5 hybrid embedded with graphitic carbon nitride nanosheets: Oxygen vacancies mediated enhanced visible-light-driven photocatalytic degradation of organic pollutants and hydrogen evolution. *Appl. Surf. Sci.* **2018**, *447*, 740−756.
(47) Li, X.; Li, M.; Yang, J.; Li, X.; Hu, T.; Wang, J.; Sui, X.; Wu, Y.; Kong, L. Synergistic effect of efficient adsorption g-C_3N_4/ZnO composite for photocatalytic property. *J. Phys. Chem. Solids* **2014**, *75*, 441−446.
(48) Hamrouni, A.; Moussa, N.; Parrino, F.; Paola, A. D.; Houas, A.; Palmisano, L. Sol−gel synthesis and photocatalytic activity of ZnO−SnO_2 nanocomposites. *J. Mol. Catal. A: Chem.* **2014**, *390*, 133−141.
(49) Yang, L.; Huang, J.; Shi, L.; Cao, L.; Zhou, W.; Chang, K.; Meng, X.; Liu, G.; Jie, Y.; Ye, J. Efficient hydrogen evolution over Sb doped SnO_2 photocatalyst sensitized by Eosin Y under visible light irradiation. *Nano Energy* **2017**, *36*, 331−340.
(50) Vattikuti, S. V. P.; Police, A. K. R.; Shim, J.; Byon, C. Sacrificial-template-free synthesis of core-shell C@Bi_2S_3 heterostructures for efficient supercapacitor and H_2 production applications. *Sci. Rep.* **2018**, *8*, No. 4194.

DOI: 10.1021/acsomega.8b00471
ACS Omega 2018, 3, 7587−7602